

RESEARCH PREPRINT

Ghosts of Softmax: Complex Singularities That Limit Safe Step Sizes in Cross-Entropy

Piyush Sao 

Oak Ridge National Laboratory, Oak Ridge, TN, USA

Abstract

Optimization analyses for cross-entropy training rely on local Taylor models of the loss: linear or quadratic surrogates used to predict whether a proposed step will decrease the objective. These surrogates are reliable only inside the Taylor convergence radius of the true loss along the update direction. That radius is set not by real-line curvature alone but by the nearest complex singularity. For cross-entropy, the softmax partition function $F = \sum_j \exp(z_j)$ has complex zeros—“ghosts of softmax”—that induce logarithmic singularities in the loss and cap this radius. Beyond it, local Taylor models need not track the true loss, so descent guarantees based on those models become unreliable.

This yields a fundamentally different constraint from L -smoothness. To make the geometry explicit and usable, we derive closed-form expressions under logit linearization along the proposed update direction. In the binary case, the exact radius is $\rho^* = \sqrt{\delta^2 + \pi^2}/\Delta_a$. In the multiclass case, we obtain the interpretable lower bound $\rho_a = \pi/\Delta_a$, where $\Delta_a = \max_k a_k - \min_k a_k$ is the spread of directional logit derivatives $a_k = \nabla z_k \cdot v$. This bound costs one Jacobian–vector product and reveals what makes a step fragile: samples that are both near a decision flip and highly sensitive to the proposed direction tighten the radius.

The normalized step size $r = \tau/\rho_a$ separates safe from dangerous updates. Across six tested architectures and multiple step directions, no model fails for $r < 1$, yet collapse appears once $r \geq 1$. Temperature scaling confirms the mechanism: normalizing by ρ_a shrinks the onset-threshold spread from standard deviation 0.992 to 0.164. A controller that enforces $\tau \leq \rho_a$ survives learning-rate spikes up to 10,000 \times in our tests, where gradient clipping still collapses. As a proof of concept, a controller that sets $\eta = r \rho_a / \|v\|$ from local geometry alone reaches 85.3% accuracy on ResNet-18/CIFAR-10 without a hand-designed learning-rate schedule (best fixed rate: 82.6%). Together, these results identify a geometric constraint on cross-entropy optimization—one that operates through Taylor convergence rather than Hessian curvature—and provide a tractable, optimizer-agnostic bound that makes it visible.

Keywords: cross-entropy; convergence radius; learning rate; partition-function zeros; training stability

Reproducibility resources. Accompanying code, notebooks, and tutorials will be available at github.com/piyush314/ghosts-of-softmax.

1. Introduction

Cross-entropy training works well but can fail suddenly. Loss spikes have been reported in large-scale runs [1, 2], and a learning rate that works early can diverge later. Practitioners mitigate these spikes with heuristics: restarting from checkpoints [1], manual intervention [2], gradient

This manuscript has been authored by UT-Battelle, LLC under Contract No. DE-AC05-00OR22725 with the U.S. Department of Energy. The publisher, by accepting the article for publication, acknowledges that the United States Government retains a non-exclusive, paid-up, irrevocable, world-wide license to publish or reproduce the published form of this manuscript, or allow others to do so, for United States Government purposes. The Department of Energy will provide public access to these results of federally sponsored research in accordance with the DOE Public Access Plan (<http://energy.gov/downloads/doe-public-access-plan>).

A Single Step Can Wipe Learned Accuracy

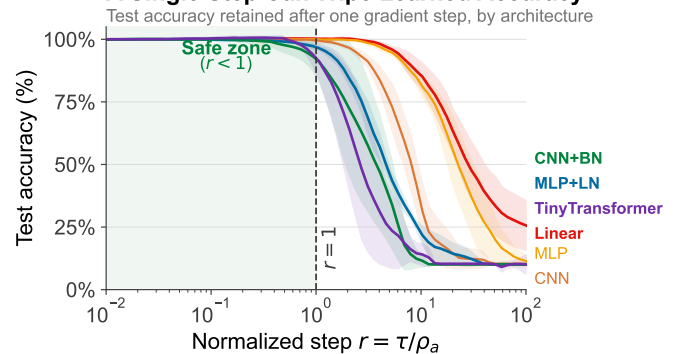


Figure 1. We train six small architectures to convergence, then take one step at varying ratios $r = \tau/\rho_a$, where τ is the step distance and ρ_a is our stability bound (defined in the text). Every network keeps its accuracy for $r < 1$; once r crosses 1, collapse appears across all six architectures.

clipping [3, 4], learning rate warmup and decay [5], or temperature scaling [6, 7].

These heuristics help, but they treat symptoms, not

causes. Clipping limits gradient magnitude, not step safety. Learning rate scheduling reduces the rate globally, slowing training everywhere. Standard L -smoothness theory misses the key case: it assumes the gradient is Lipschitz with constant L and, for $\eta < 2/L$, guarantees descent. Yet for cross-entropy this bound hides a late-training failure mode. Figure 1 shows the result: at roughly twice the later-defined bound ρ_a , accuracy collapses in one update.

We identify a geometric mechanism that existing analyses miss. Many descent analyses justify an update by studying a local Taylor polynomial of the loss. They treat this polynomial as a proxy for the true objective and show that it decreases. This reasoning is reliable only if the Taylor series converges at the update point. By Cauchy–Hadamard (Section 2), convergence holds inside the disk set by the nearest complex singularity. Inside the disk, the truncated series tracks the function, so descent results transfer. Outside the disk, the series can diverge from the function, so proving that the series decreases no longer proves that the function decreases.

For cross-entropy loss, a key mechanism is the softmax partition function. Along the step direction, the loss equals $\log(\sum_k \exp z_k(\theta + \tau\nu))$. This sum stays positive for real τ but has zeros in the complex plane. Those zeros induce off-axis logarithmic singularities—“ghosts”—that still cap the convergence radius. As training sharpens predictions, the logit-derivative spread Δ_a often grows, moving ghosts toward the origin and shrinking the safe step size. This tightening occurs even when L -smoothness permits larger nominal steps.

For softmax cross-entropy, linearizing the logits along the step direction yields the closed-form lower bound $\rho_a = \pi/\Delta_a$, where $\Delta_a = \max_k a_k - \min_k a_k$ is the logit-derivative spread for $a_k = \nabla z_k \cdot \nu$. Linearization is not needed for the mechanism; it is needed for a cheap and interpretable bound. Without it, one can use numerical methods to locate the nearest complex singularity. This first-order proxy is useful not only because it is computable (one JVP), but because it shows which quantity matters: Δ_a . For binary cross-entropy the exact radius is

$$\rho^* = \sqrt{\delta^2 + \pi^2} / \Delta_a,$$

where δ is the logit gap between classes; the worst case is $\delta = 0$, giving ρ_a . During training, Δ_a grows along the gradient direction, so ρ_a shrinks and a fixed learning rate eventually violates $r < 1$.

Define the normalized step size $r = \tau/\rho_a$, where $\tau = \|p\|$ is the step distance. When ρ_a is recomputed along ν at each step, $r < 1$ guarantees Taylor convergence for any optimizer direction when logits are approximately linear over the step. We confirm this direction-independence empirically: sweeping r along the gradient and 20 random

directions yields the same transition at $r \approx 1$ (Section 6, Figure 8). The bound is a reliability boundary, not a cliff: training may survive $r > 1$ when cancellation is favorable, but without a guarantee.

Our argument has three layers. First, a geometric fact: the real loss $\ell(\tau) = \mathcal{L}(f(\theta + \tau\nu))$ is analytic in a complex neighborhood of the real line, and its Taylor convergence radius is set by the nearest complex singularity—not by real curvature. This holds for any parameterization, independently of logit linearity. Second, a tractable specialization: linearizing the logits along the step direction isolates the softmax singularity structure, yielding the explicit bound $\rho_a = \pi/\Delta_a$. Linearization makes the obstruction computable and interpretable. Third, empirical evidence: this conservative lower bound is predictive enough to diagnose, explain, and prevent instability across the settings we test.

Contributions

- 1. A geometric constraint on optimization (Sections 2–4).** The real loss $\ell(\tau) = \mathcal{L}(f(\theta + \tau\nu))$ along any update direction ν is analytic, and its Taylor convergence radius is set by the nearest complex singularity of ℓ . For cross-entropy, the softmax partition function $\sum_k \exp z_k(\tau)$ has complex zeros that induce logarithmic singularities in the loss. Beyond this radius, polynomial models of the loss can diverge from the function itself, so descent guarantees built on those models lose validity. This constraint operates through Taylor convergence geometry, not Hessian curvature, and tightens as predictions sharpen—even when the real loss surface appears increasingly flat.
- 2. A tractable lower bound (Theorems 4.3–4.6).** Linearizing the logits isolates the softmax singularity structure and yields $\rho_a = \pi/\Delta_a$, computable via one Jacobian-vector product. For binary cross-entropy the exact radius is $\rho^* = \sqrt{\delta^2 + \pi^2}/\Delta_a$. Linearization makes the softmax obstruction computable by revealing the controlling variable Δ_a . A separate proof via real-variable KL divergence bounds confirms the same $O(1/\Delta_a)$ scaling (section Appendix 4).
- 3. Empirical validation (Sections 5–6).** Across six architectures and multiple update directions, the normalized step $r = \tau/\rho_a$ separates safe from failing updates: no tested model fails for $r < 1$. Temperature scaling collapses the spread of failure-onset thresholds across architectures from $\sigma = 0.992$ to 0.164. As a proof of concept, a controller that caps $\tau \leq \rho_a$ survives 10,000× learning-rate spikes where gradient clipping collapses, and on ResNet-18/CIFAR-10 reaches 85.3% without a hand-designed schedule (best fixed rate: 82.6%).

This paper establishes the one-step singularity constraint for softmax and provides a tractable bound. Multi-step dynamics, activation singularities, and computational optimization are natural extensions that build on this foundation (sections Appendix 2 and 8).

Section 2 reviews the complex-analytic foundations. Section 3 formulates the problem. Section 4 derives the convergence radius. Sections 5–6 apply and validate the framework. Section 8 discusses implications and limitations.

2. Preliminaries

This section develops a central insight used throughout the paper: many optimization analyses and heuristics rely on local Taylor models, but those models are reliable only within a convergence region that simple quadratic approximations do not capture. We introduce concepts from complex analysis to characterize this region and show how it constrains optimization.

2.1 Analytic Functions and Taylor Series

A function $f : \mathbb{R} \rightarrow \mathbb{R}$ is *analytic* at x_0 if it equals its Taylor series in some neighborhood:

$$f(x) = \sum_{n=0}^{\infty} \frac{f^{(n)}(x_0)}{n!} (x - x_0)^n, \quad |x - x_0| < R \quad (1)$$

for some radius $R > 0$, and truncating at order n then yields an approximation with controlled error. This justifies finite-derivative models such as linear ($n = 1$) and quadratic ($n = 2$, as in L -smoothness) approximations.

2.2 A Simple Example: $f(x) = 1/(x + a)$

To see how the convergence radius limits Taylor approximations, consider $f(x) = 1/(x+a)$ for $a > 0$. On the positive reals, f is smooth, bounded, and monotone; its singularity lies at $x = -a$ on the negative half-line. The Taylor series around $x_0 = 0$ is:

$$f(x) = \frac{1}{a} \sum_{n=0}^{\infty} \left(-\frac{x}{a}\right)^n = \frac{1}{a} - \frac{x}{a^2} + \frac{x^2}{a^3} - \dots \quad (2)$$

This converges only for $|x| < a$. Yet at $x = 2a$ —outside this range—the function is perfectly well-defined: $f(2a) = 1/(3a)$. The Taylor series diverges; partial sums oscillate and grow in magnitude. In fact, no finite truncation approximates $f(2a)$, and the error can grow with truncation order (Figure 2).

2.2.1 When does this divergence occur?

Why does the singularity at $x = -a$ affect the series at $x = 2a$? Along the real line, the singularity seems far away

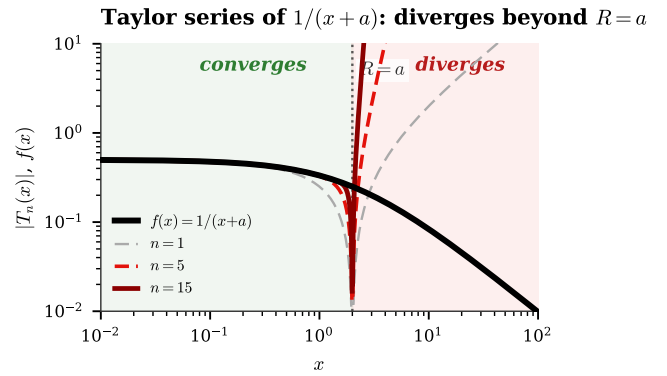


Figure 2. Taylor approximations $T_n(x)$ of $f(x) = 1/(x + a)$ around $x_0 = 0$. Inside the convergence radius $R = a$ (green), all orders approximate f well. Beyond R (red), higher-order approximations diverge faster, not slower.

Complex Singularity at $i\pi$ Bounds Taylor Series to $|x| < \pi$

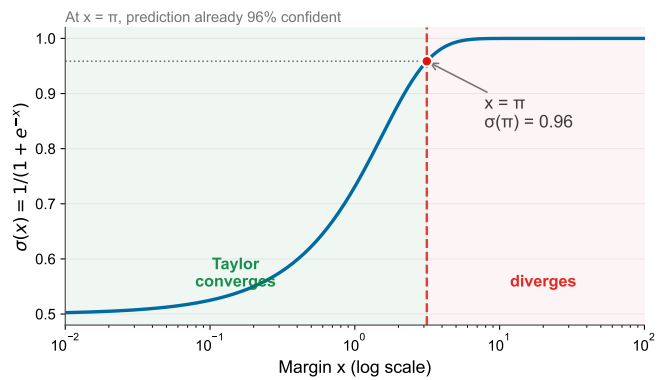


Figure 3. Binary cross-entropy’s log-partition $\log(1 + e^x)$ has convergence radius $\rho = \pi$ set by the complex zero at $i\pi$ (Euler: $1 + e^{i\pi} = 0$). Shown: derivative $\sigma(x)$ on log scale. Green: Taylor converges ($|x| < \pi$). Red: diverges ($|x| > \pi$).

and the function is smooth in between. The answer lies in the complex plane.

Theorem 2.1 (Cauchy–Hadamard). *The Taylor series of f around x_0 converges for $|x - x_0| < R$, where R is the distance from x_0 to the nearest point where f fails to be analytic (a singularity) [8]. The series diverges for $|x - x_0| > R$.*

For $f(x) = 1/(x + a)$, the complex extension $f(z) = 1/(z + a)$ has a pole at $z = -a$. From the expansion point $z_0 = 0$, this pole lies at distance a , so the convergence disk has radius a . The radius is determined by the complex singularity, not by the function’s behavior on the real line.

2.2.2 Implications for neural networks

This analyticity principle has practical consequences. The binary log-partition $\log(1 + e^x)$ is smooth on \mathbb{R} and has no real singularities, yet its Taylor series diverges for $|x| > \pi$. The reason lies in the complex plane: Euler’s identity gives

$1 + e^{i\pi} = 0$, so the function vanishes at $x = i\pi$, creating a branch point of the logarithm. This purely imaginary singularity limits the convergence radius to π (Figure 3).

Key insight. A singularity need not lie between the expansion and evaluation points, nor must it lie on the real line. If a singularity lies within distance R of the expansion point in the complex plane, the Taylor series diverges beyond R in every direction. This leads to the optimization question: when does an update step exceed the convergence radius?

2.3 Optimization and the Convergence Radius

Any analysis that extrapolates local derivatives to predict finite-step behavior faces the same limitation. We now make it precise for directional steps.

2.3.1 Taylor expansion of the update

Let $f : \mathbb{R}^n \rightarrow \mathbb{R}$ be analytic, with gradient $g = \nabla f(x)$ and Hessian $H = \nabla^2 f(x)$ at the current iterate x . An optimizer chooses a step p (e.g. $p = -\eta g$ for gradient descent, or a pre-conditioned direction for Adam). The Taylor expansion around x for any step p is:

$$f(x + p) = f(x) + g^\top p + \frac{1}{2} p^\top H p + O(\|p\|^3). \quad (3)$$

For gradient descent ($p = -\eta g$) this becomes:

$$f(x - \eta g) = f(x) - \eta \|g\|^2 + \frac{1}{2} \eta^2 g^\top H g + O(\eta^3 \|g\|^3). \quad (4)$$

The first-order term $-\eta \|g\|^2$ suggests descent. The second-order term captures curvature along g , explaining why large η can fail. But the key constraint applies to any step p : the expansion is valid only when it converges.

2.3.2 The implicit assumption

Equation (4) gives a local expansion. To use this approximation at a finite step, we must control higher-order terms. For analytic $h(t) = f(x + tu)$ with $u = p/\|p\|$, let ρ be the convergence radius of the Taylor series around $t = 0$. By Cauchy–Hadamard, series convergence requires:

$$\|p\| < \rho. \quad (5)$$

For gradient descent ($p = -\eta g$), this yields $\eta < \rho/\|g\|$ along direction $u = -g/\|g\|$. More generally:

$$\boxed{\|p\| < \rho} \quad (6)$$

When the gradient is large (far from a stationary point), the permissible step size shrinks. This is a separate mechanism from curvature-based bounds: the local polynomial model itself becomes unreliable.

2.3.3 Inside vs. outside the radius

This unreliability is not gradual—the convergence radius ρ creates a sharp dichotomy:

- **Inside** ($\|p\| < \rho$): The Taylor series converges. Adding terms improves accuracy.
- **Outside** ($\|p\| > \rho$): The Taylor series diverges. Adding terms need not improve the approximation and can make it *worse* (Figure 2).

This is not a failure of finite precision or truncation error. It is a fundamental limitation: once singularities limit convergence, derivatives at x do not fully encode behavior at the update point.

2.3.4 Curvature versus convergence radius

This fundamental limit differs from the familiar curvature-based bound. Standard analysis uses the Lipschitz constant L of the gradient to bound step size, yielding $\eta < 2/L$. This curvature-based bound reflects how rapidly the gradient changes. In contrast, the convergence radius ρ imposes a separate, often stricter limit based on *analyticity*: where the Taylor representation breaks down entirely.

For functions like $f(x) = 1/(x+a)$, the Hessian $f''(x) = 2/(x+a)^3$ shrinks as x grows, suggesting that large steps are safe. Yet the convergence radius remains $\rho = x+a$, forbidding steps that cross the singularity. Curvature-based analysis misses this barrier; for cross-entropy, the mismatch grows exponentially with confidence (Section 5).

2.3.5 Directional convergence radius

So far we have treated the convergence radius as a scalar, but optimization steps follow specific directions. Let u be any unit direction in parameter space. The *directional convergence radius* along u is:

$$\boxed{\rho_u = \sup\{t > 0 : \text{Taylor series converges at } x + tu\}} \quad (7)$$

This gives the constraint $\|p\| < \rho_u$ where $u = p/\|p\|$. Different directions have different radii, determined by singularities in f 's complex extension. The gradient direction maximizes first-order decrease, not ρ_u , so these objectives may conflict.

What remains. The preceding argument explains *why* the convergence radius matters: beyond it, no finite polynomial model guarantees local fidelity. What remains is to *compute* it. For cross-entropy, the bottleneck is a log-partition zero at imaginary distance proportional to π (Figure 3). The next section derives a computable lower bound on this radius and shows how to use it.

3. Problem Formulation

We compute the radius of convergence for a given update direction. Along that direction, this radius measures the distance to the nearest complex singularity of the loss. Practically, it gives the maximum safe step size implied by derivative information. We now formulate the problem and identify the function whose zeros determine this radius.

3.1 Model, Loss, and Movement

To analyze the loss trajectory, we first define the model outputs and update scheme.

3.1.1 The model and logits

A neural network f_θ maps input x and parameters θ to raw, unnormalized scores called *logits*:

$$z = f_\theta(x) \in \mathbb{R}^n$$

where n is the number of classes and z_k is the score for class k .

3.1.2 Cross-entropy loss

For a target class y , the loss is the negative log-probability of that class:

$$\mathcal{L} = -\log \text{softmax}_y(z) = -z_y + \log \sum_{k=1}^n e^{z_k}$$

The first term $-z_y$ is the correct-class logit. The second term $\log \sum_k e^{z_k}$ is the *log-partition function*—it normalizes probabilities and introduces the nonlinearity whose behavior depends on the step direction.

3.1.3 The optimizer step

To minimize loss, we update parameters by taking a step τ along a unit direction ν :

$$\theta(\tau) = \theta_0 + \tau\nu$$

where θ_0 is the current parameters, ν is any unit vector in parameter space (e.g. the negative normalized gradient, a normalized Adam update, or a random direction), and τ is the step distance.

3.1.4 The 1D loss landscape

We restrict analysis to the line defined by this step. Define the scalar function $\ell(\tau)$ as the loss at distance τ :

$$\ell(\tau) = \mathcal{L}(\theta_0 + \tau\nu)$$

Our goal is to determine the maximum τ for which a Taylor series of $\ell(\tau)$ converges.

3.2 The Logit Linearization Assumption

Because the loss landscape is nonlinear, we approximate logits as linear in the step size. This requires computing how each logit changes with the step.

3.2.1 Jacobian-vector product

The rate of change of logit k along direction ν is

$$a_k = \left. \frac{dz_k}{d\tau} \right|_{\tau=0} = (\nabla_\theta z_k) \cdot \nu$$

For all classes simultaneously, this becomes a Jacobian-vector product:

$$a = J_z \cdot \nu \in \mathbb{R}^n$$

where $J_z = \partial z / \partial \theta$ is the Jacobian matrix containing all partial derivatives of logits with respect to parameters.

3.2.2 Core assumption: linearized logits

We assume logits change linearly for small steps:

$$z_k(\tau) \approx z_k(0) + a_k\tau$$

Substituting into the loss yields the approximated 1D loss:

$$\ell(\tau) = -z_y(0) - a_y\tau + \log \sum_{k=1}^n e^{z_k(0) + a_k\tau}$$

Define weights $w_k = e^{z_k(0)} > 0$ from the initial logits. The loss simplifies to

$$\ell(\tau) = -a_y\tau + \log F(\tau) + \text{const}$$

where

$$F(\tau) = \sum_{k=1}^n w_k e^{a_k\tau} \quad (8)$$

is the *partition function* along the step direction.

3.2.3 The radius from partition zeros

Only $\log F(\tau)$ in $\ell(\tau)$ can diverge, which happens when $F(\tau) = 0$. The linear term $-a_y\tau$ has no singularities, so divergence depends entirely on whether F can vanish. For real τ , all terms are positive, so $F(\tau) > 0$. However, zeros can occur for complex τ . By Cauchy–Hadamard, the convergence radius is determined by these complex zeros:

$$\rho = \min\{|\tau| : F(\tau) = 0, \tau \in \mathbb{C}\}$$

This is the central result of this section: under the linearization assumption, the convergence radius equals the magnitude of the nearest complex zero of the partition function. Any step $\tau < \rho$ lies within the region where derivative information reliably predicts the loss, so ρ is the maximum safe step size implied by the local Taylor model.

Sign invariance. This quantity depends on the directional derivatives a_k but not on the sign convention for the step: using $\theta_0 - \tau v$ flips all a_k signs, but $\Delta_a = \max_k a_k - \min_k a_k$ and all radius bounds are invariant.

4. The Convergence Radius

Section 3 showed that the convergence radius is determined by zeros of the partition function $F(\tau) = \sum_k w_k e^{a_k \tau}$. We now derive this radius step by step: first the exact value ρ^* , then a closed form for binary classification, then a per-sample lower bound π/Δ_a , and finally batch and dataset bounds.

4.1 Definition of ρ^*

Definition 4.1 (Exact Convergence Radius). For a loss function f at parameters θ with unit update direction v , the *exact convergence radius* is the convergence radius of $\ell(t) = f(\theta + tv)$ at $t = 0$. By the Cauchy–Hadamard theorem, this equals the distance from the origin to the nearest singularity of ℓ 's analytic continuation to \mathbb{C} .

This definition applies to any loss; for cross-entropy specifically, the singularities come from zeros of the partition function F (equivalently, singularities of $\log F$).

Proposition 4.2 (Radius from Partition Zeros). For cross-entropy loss with partition function $F(t) = \sum w_k e^{a_k t}$ (where $w_k > 0$), the exact radius is

$$\rho^* = \min\{|t| : F(t) = 0\} \quad (9)$$

Proof. The loss is $\ell(t) = -z_y(t) + \log F(t)$. The linear term $-z_y(t)$ is entire; singularities come only from $\log F$, which has branch points where $F = 0$. If F is nonzero on $|t| \leq R$, then $\log F$ is holomorphic there. At a zero t_0 with $|t_0| = \rho^*$, $\log F$ has a branch point, so the radius is exactly ρ^* . \square

Notation. In this section, t denotes the possibly complex step parameter (elsewhere written τ for real steps). With this convention, we exploit complex analysis to find ρ^* in closed form—starting with binary classification.

4.2 Binary Classification: Exact Formula

For binary classification, we can compute ρ^* in closed form. Let $\Delta_a = |a_1 - a_2|$ be the logit-derivative spread and $\delta = z_1(0) - z_2(0)$ the logit gap.

Theorem 4.3 (Binary Convergence Radius). For $F(t) = w_1 + w_2 e^{\Delta_a t}$ with $w_1, w_2 > 0$, spread $\Delta_a = |a_1 - a_2|$, and logit gap $\delta = \log(w_1/w_2)$:

$$\rho^* = \frac{\sqrt{\delta^2 + \pi^2}}{\Delta_a} \quad (10)$$

The minimum $\rho^* = \pi/\Delta_a$ occurs when $\delta = 0$ (balanced).

Proof. $F(t) = 0$ requires $e^{\Delta_a t} = -w_1/w_2$. Taking the complex logarithm:

$$\Delta_a t = \log(w_1/w_2) + i\pi(2k+1) = \delta + i\pi(2k+1)$$

The nearest zeros (at $k = 0, -1$) lie at distance $|t| = \sqrt{\delta^2 + \pi^2}/\Delta_a$. \square

The formula reveals two contributions to the radius:

- The imaginary part π/Δ_a is confidence-independent: it is set by $e^{i\pi} = -1$, the condition for exponential sums to cancel. Even a balanced prediction ($\delta = 0$) has finite radius.
- The real part δ/Δ_a grows with confidence: large margins shift the zero away from the imaginary axis, making confident predictions more robust to large steps.

4.3 Per-Sample Lower Bound

For multi-class classification, exact computation of ρ^* requires finding zeros of $F(t) = \sum_{k=1}^n w_k e^{a_k t}$, which lacks a closed form for $n > 2$. We derive a lower bound for a single sample along a single direction, then aggregate to batches and datasets.

Definition 4.4 (Logit-Derivative Spread). Along direction v , define the logit JVP $a(x; v) = J_{z(x)} v$ and the *per-sample logit-derivative spread*

$$\Delta_a(x; v) = \max_k a_k - \min_k a_k. \quad (11)$$

4.3.1 Proof: $\rho^*(x; v) \geq \pi/\Delta_a(x; v)$

We show that no zero of $F(t) = \sum w_k e^{a_k t}$ lies within distance π/Δ_a of the origin. For $n > 2$ classes, the zeros have no closed form, so algebraic methods do not apply. Instead, we use a geometric argument: when $|t|$ is small, all terms of $F(t)$ lie in the same open half-plane and cannot cancel.

Lemma 4.5 (Half-Plane Obstruction). If complex numbers u_1, \dots, u_n have arguments in an open arc of length $< \pi$, then $\sum c_k u_k \neq 0$ for any $c_k > 0$.

Proof. Let ϕ bisect the arc. Then $\text{Re}(e^{-i\phi} u_k) > 0$ for all k , so $\text{Re}(e^{-i\phi} \sum c_k u_k) > 0$. \square

Figure 4 visualizes this geometry: vectors confined to an open half-plane share a projection direction with positive real part, so no positive combination can produce zero.

Theorem 4.6 (General Lower Bound). For $F(t) = \sum w_k e^{a_k t}$ with $w_k > 0$:

$$\rho^* \geq \frac{\pi}{\Delta_a} \quad (12)$$

where $\Delta_a = \max_k a_k - \min_k a_k$.

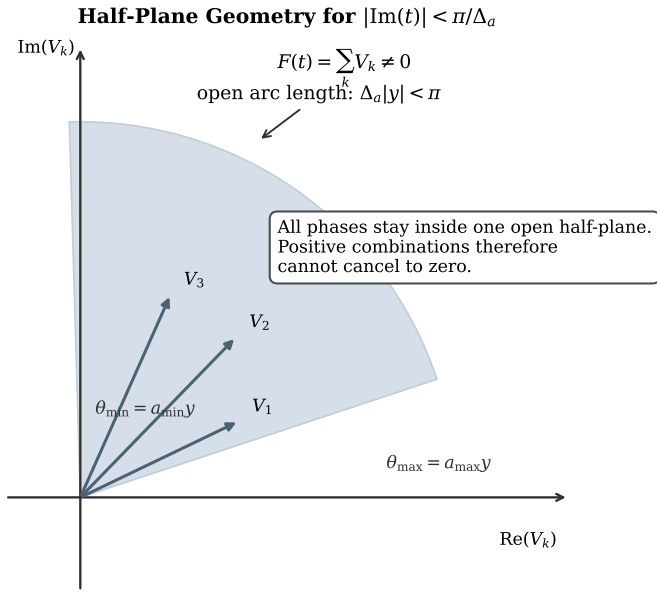


Figure 4. Half-plane geometry behind Lemma 4.5. If the phases of $V_k = w_k e^{a_k t}$ lie in an open arc of length $< \pi$, then all vectors remain in a common open half-plane, so no positive combination can cancel to zero.

Complex- t Consequence: Forbidden Strip and Radius Bound

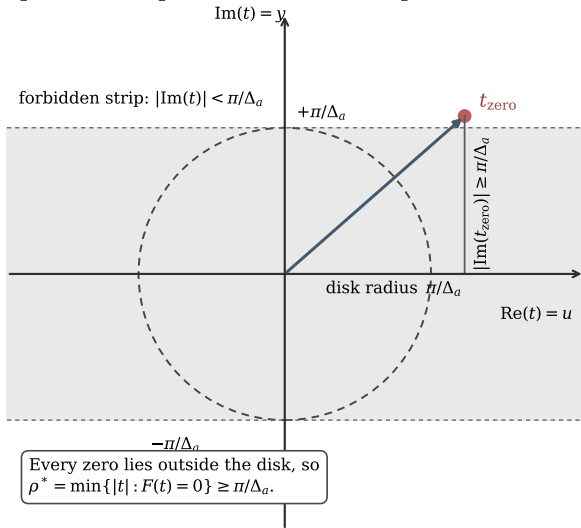


Figure 5. Complex- t consequence of Theorem 4.6. The half-plane obstruction excludes zeros from the strip $|\text{Im}(t)| < \pi/\Delta_a$. Since the disk $|t| < \pi/\Delta_a$ lies inside that strip, the minimal zero modulus satisfies $\rho^* \geq \pi/\Delta_a$.

Proof. Let $t = u + iy$, where $u = \text{Re}(t)$ and $y = \text{Im}(t)$. Each term $w_k e^{a_k t}$ has phase $a_k y$, because $w_k e^{a_k u} > 0$ contributes only magnitude. If $\Delta_a |y| < \pi$, all phases lie in an arc of length $< \pi$. By Lemma 4.5, $F(t) \neq 0$. Therefore any zero satisfies $|\text{Im}(t)| \geq \pi/\Delta_a$, giving $|t| \geq \pi/\Delta_a$. \square

Figure 5 shows the same implication in the complex t plane: the strip $|\text{Im}(t)| < \pi/\Delta_a$ is zero-free, and the disk $|t| < \pi/\Delta_a$ lies entirely inside it. How tight is this bound?

For confident predictions ($|\delta|$ large) or multi-class problems, the bound is conservative, but for binary classification at $\delta = 0$ it is tight: $\rho^* = \pi/\Delta_a$.

4.3.2 Per-sample ghosts

Applying Theorem 4.6 to a single sample x gives $\rho(x; \nu) \geq \pi/\Delta_a(x; \nu)$. Each sample has a ghost—a complex singularity determined by its logits and directional slopes. For multiclass samples, exact ghost locations are roots of $F_x(t) = \sum_k w_k(x) e^{a_k(x; \nu) t}$ and generally have no closed form, but can be computed numerically for any given sample. In the binary case, or under a top-2 reduction with margin $\delta(x) = z_\gamma - z_c$ and top-2 derivative gap $\Delta_{\gamma,c}(x; \nu) = a_\gamma - a_c$, the nearest ghost is

$$\tau_{\text{ghost}}(x; \nu) = \frac{\delta(x) + i\pi}{\Delta_{\gamma,c}(x; \nu)}, \quad \rho(x; \nu) = \frac{\sqrt{\delta(x)^2 + \pi^2}}{|\Delta_{\gamma,c}(x; \nu)|}. \quad (13)$$

This formula explains why π/Δ_a is conservative: confident samples ($|\delta|$ large) have exact radii exceeding the bound by a factor of $\sqrt{1 + (\delta/\pi)^2}$, while low-margin samples lie near the boundary.

4.4 Batch and Dataset Bounds

Each training step updates all samples simultaneously. To ensure safety, τ must satisfy $\tau < \min_x \rho(x; \nu)$. From Theorem 4.6, we have $\rho(x; \nu) \geq \pi/\Delta_a(x; \nu)$. This yields the conservative sufficient condition $\tau < \pi/\max_x \Delta_a(x; \nu)$. The bottleneck sample—the one with largest Δ_a —determines the safe step size.

Definition 4.7 (Computable Radius Bound). For a sample set \mathcal{S} , the Δ_a -based radius bound is

$$\rho_a(\nu) = \frac{\pi}{\max_{x \in \mathcal{S}} \Delta_a(x; \nu)} \quad (14)$$

Notation conventions. When arguments are omitted, ν defaults to the gradient direction $\nabla f / \|\nabla f\|$, and the sample set defaults to the full training set \mathcal{D} . Thus $\Delta_a(x) = \Delta_a(x; \nabla f / \|\nabla f\|)$ and $\rho_a = \pi / \max_{x \in \mathcal{D}} \Delta_a(x)$. Restricting to a mini-batch $\mathcal{B} \subseteq \mathcal{D}$ gives a less conservative bound $\rho_{\mathcal{B}} \geq \rho_a$, since the maximum over fewer samples is smaller. In general:

$$\rho_a \leq \rho_{\mathcal{B}} \leq \rho(x; \nu) \quad \text{for any } x \in \mathcal{B} \quad (15)$$

The training-set bound ρ_a is the most conservative; the per-sample bound $\rho(x; \nu)$ is the least. In practice, the bottleneck samples that drive ρ_a down are those with small top-2 margins, whose nearest ghosts lie closest to the real axis.

4.5 Computing $\Delta_a(x; v)$

We now turn to practical computation. Computing $\Delta_a(x; v)$ requires one forward-mode automatic differentiation (AD) pass (a Jacobian–vector product) per sample:

1. Compute update direction $v = \nabla f / \|\nabla f\|$
2. For each sample x , compute $a(x; v) = J_{z(x)} v$
3. Return $\Delta_a(x; v) = \max_k a_k - \min_k a_k$

Cost: each JVP is comparable to one forward pass ($\sim 1.5\times$ overhead). Since only the bottleneck sample determines ρ_a , total cost for a batch of B samples is approximately $1.5B$ forward passes.

Summary. We defined the exact radius ρ^* and derived its closed form for binary classification. We then established the computable bound $\rho_a(v) = \pi / \max_x \Delta_a(x; v)$ and proved that $\rho^* \geq \rho_a$. Section 5 shows how to use this bound to predict and prevent instability.

5. Using the Radius

Section 4 established that the Taylor expansion converges only when the step distance does not exceed the convergence radius. For any direction v :

$$\boxed{\tau < \rho(v)} \quad (16)$$

where $\tau = \|p\|$ is the step distance and $\rho(v)$ is the convergence radius, satisfying $\rho(v) \geq \rho_a(v) = \pi / \max_x \Delta_a(x; v)$. We now define a normalized step size, interpret it as a learning-rate constraint, and design a controller that enforces the bound.

5.1 The Normalized Step Size

Let p be the parameter update from any optimizer, with $v = p / \|p\|$ as the unit step direction. Both the step distance $\tau = \|p\|$ and the radius $\rho_a(v) = \pi / \Delta_a(v)$ are measured along v , with

$$\Delta_a(v) = \max_{x \in \mathcal{S}} \left(\max_k a_k(x; v) - \min_k a_k(x; v) \right), \quad a(x; v) = J_{z(x)} v.$$

Here \mathcal{S} is the sample set used by the controller (mini-batch or full training set). The ratio of step distance to radius is dimensionless:

Definition 5.1 (Normalized Step Size).

$$\boxed{r(v) = \frac{\tau}{\rho_a(v)} = \frac{\|p\| \cdot \Delta_a(v)}{\pi}} \quad (17)$$

where v is any unit optimizer direction, $\|p\|$ is the step norm, and $\Delta_a(v)$ is the set-maximum spread defined above. For gradient descent, $v = \nabla f / \|\nabla f\|$ and $\|p\| = \eta \|\nabla f\|$, recovering $r = \eta \|\nabla f\| \cdot \Delta_a / \pi$.

Like a power series $\sum a_n x^n$ with radius R , $r < 1$ ensures convergence under the conservative bound ρ_a . Because r normalizes by the local radius, it is architecture-independent: it measures the step in natural units set by local loss geometry. Its value partitions optimizer behavior into three regimes:

- $r < 1$: Taylor series converges; polynomial model is reliable
- $r \approx 1$: boundary regime; error bound diverges
- $r > 1$: Taylor series may diverge; finite-order approximations lose guarantees

5.2 Learning Rate as Geometric Constraint

The condition $r < 1$ can be rewritten as

$$\eta < \frac{\rho_a}{\|\nabla f\|} = \frac{\pi}{\Delta_a \|\nabla f\|} \quad (18)$$

Rather than being tuned freely, the learning rate is upper-bounded at each step by local analytic structure.

One might ask whether adaptive optimizers already enforce this bound. Adam scales updates by inverse gradient moments, addressing per-parameter scale differences. This is distinct from the radius constraint, which bounds the *global* step distance τ . A flat Hessian (small gradient moments) does not imply a large radius; the ghosts remain at fixed imaginary distance π .

5.3 A ρ -Adaptive Controller

Standard optimizers like Adam ignore the radius bound: they scale updates by gradient moments, so as ρ_a shrinks during training (Section 6), they keep using step sizes that worked earlier until they cross the boundary and diverge.

Can we build a practical controller that enforces $\tau \leq \rho_a$? The requirements are: (1) compute ρ_a efficiently, (2) modulate the step without new hyperparameters, and (3) generalize across architectures.

Design. A simple norm clip directly enforces the conservative safety condition.

Proposition 5.2 (Radius Clip Enforces $r \leq 1$). *Let p be a tentative optimizer update, with $\tau_0 = \|p\|$ and $v = p / \|p\|$. Define*

$$s = \min\left(1, \frac{\rho_a(v)}{\tau_0}\right), \quad \tilde{p} = s p.$$

Then $\|\tilde{p}\| \leq \rho_a(v)$ and therefore $r(v) = \|\tilde{p}\| / \rho_a(v) \leq 1$.

Proof.

$$\|\tilde{p}\| = s \tau_0 = \min(\tau_0, \rho_a(v)) \leq \rho_a(v).$$

Divide by $\rho_a(v)$. □

In practice, the controller rescales the tentative optimizer update:

$$s = \min(1, \rho_a / \|p\|), \quad \tilde{p} = s p \quad (19)$$

where $\|p\|$ is the optimizer update norm (the Adam direction times the base learning rate) and $\rho_a = \pi / \Delta_a$ is computed via one JVP along the actual optimizer direction v . No additional hyperparameters are required.

Framing. This controller is a proof of concept, not a production optimizer. It shows that ρ alone contains enough information to determine a conservative safe step size, without requiring manual retuning.

6. Experimental Validation

The preceding sections derived a stability bound ($r < 1$) and designed an adaptive controller. Three questions remain open: (1) Does $r = 1$ actually predict failure across architectures and directions? (2) Does the theory correctly predict how temperature and other parameters shift the boundary? (3) Does r track instabilities in realistic, unperturbed training? We address these progressively, moving from controlled single-step tests to multi-step training and from artificial perturbations to natural instabilities.

6.1 Learning Rate (LR) Spike Tests

We begin with the most controlled setting: injecting a known LR spike and asking whether $r = 1$ predicts the outcome. We sweep learning rates over four orders of magnitude while injecting a 1000× spike.

We use a two-layer multilayer perceptron (MLP; $64 \rightarrow 128 \rightarrow 10$) for digit classification with Adam and custom step-size control. At step 50, the base learning rate is multiplied by 1000× and held for 150 more steps.

Figure 6 shows three regimes:

$\eta_0 = 10^{-4}$ (row 1): The spike raises the effective learning rate to 0.1, which remains within ρ_a . Both methods are indistinguishable. The right panel confirms that τ stays in the green safe region.

$\eta_0 = 10^{-3}$ (row 2): Post-spike LR is 1.0. Plain Adam’s accuracy drops to $\sim 50\%$, never recovering. The right panel shows τ exceeding ρ_a by $\sim 10\times$.

$\eta_0 = 10^{-2}$ (row 3): Post-spike LR is 10. Plain Adam diverges—accuracy drops to chance. The right panel shows τ exceeding ρ_a by $\sim 100\times$.

The ρ_a -controller (gold) survives all spikes by capping $\tau \leq \rho_a$. This is a controlled perturbation by design; the following subsections test whether the boundary generalizes.

6.2 Cross-Architecture Validation

Having established that $r = 1$ predicts spike-induced failure on a single architecture, we ask whether the boundary holds more broadly. Figure 7 sweeps r from 0.01 to 100 on six architectures via single gradient steps on converged models. The key result is that **no tested architecture fails for $r < 1$** . Multi-step dynamics are examined in Sections 6.7–6.6.

Phase transitions cluster between $r = 1$ and $r = 10$. This slack reflects confidence-margin slack: the exact radius $\rho^* = \sqrt{\delta^2 + \pi^2} / \Delta_a$ (Theorem 4.3) exceeds the conservative bound $\rho_a = \pi / \Delta_a$ whenever the logit gap satisfies $|\delta| > 0$. Confident predictions therefore extend the safe region beyond the conservative bound. Before testing this quantitatively, we first verify that r is direction-independent.

6.3 Random-Direction Validation

The previous tests perturbed along the gradient. Since $\rho_a = \pi / \Delta_a$ depends on direction through Δ_a , we test whether normalizing by this direction-specific radius yields a universal coordinate. Figure 8 sweeps r along the gradient and along 20 random directions at three training phases.

Both metrics—loss ratio (post-step loss divided by pre-step loss) and flip fraction (proportion of predictions that change class)—transition near $r \approx 1$ regardless of direction. The gradient direction is the extreme case: at the same r , it shows earlier degradation than random directions. Adversarial directions that minimize ρ_a for fixed τ remain unexplored. Nevertheless, the direction-dependent slack confirms that ρ_a is a conservative bound across all tested directions.

6.4 Temperature-Scaling Fingerprint

The preceding tests confirmed the bound’s shape; we now test a quantitative prediction. Temperature rescales logits as z/T , so the predicted radius rescales as $\rho_a(T) = \pi T / \Delta_a$. Figure 9 tests this prediction directly. In raw τ coordinates (panel A), collapse onsets vary widely across temperatures (collapse std = 0.992). After theory normalization by T (panel B), those onsets collapse to a common transition (std = 0.164, a 6× reduction).

This is a mechanistic check, not just a fit: changing T shifts the boundary in the direction and magnitude predicted by the analytic bound. The remaining spread is expected from confidence-margin slack ($\rho^* > \rho_a$ for confident samples) and nonlinear deviations from logit linearization.

6.5 Controller Across Architectures

Having validated the bound’s shape, direction-independence, and temperature scaling, we return to the controller. Ex-

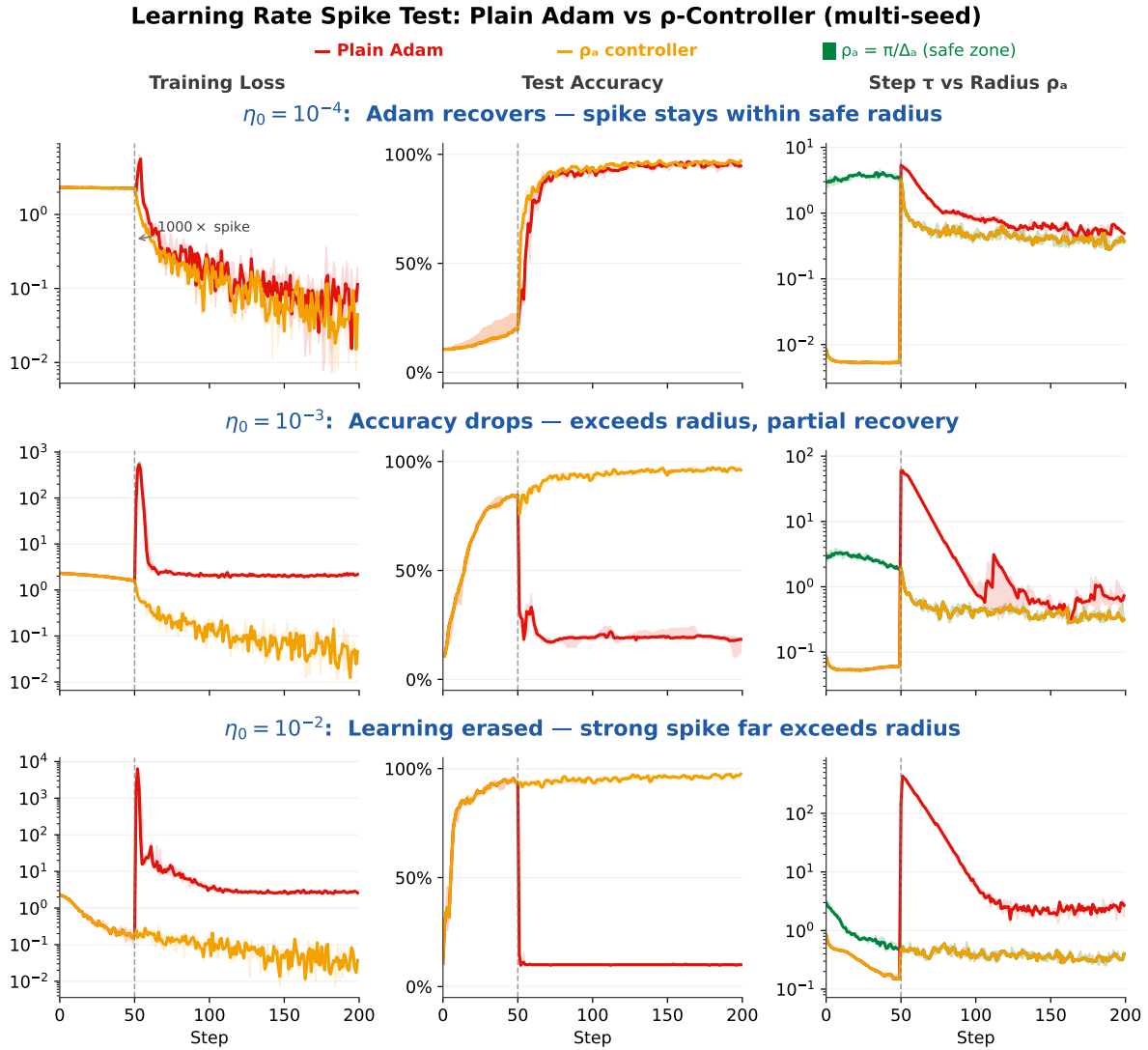


Figure 6. Learning rate spike test (5 seeds, median with interquartile range (IQR) bands). Each row uses a different base LR. **Left:** training loss. **Center:** test accuracy. **Right:** step size τ vs radius ρ_a (green = safe zone). Row 1: spike stays within ρ_a , Adam recovers. Row 2: τ exceeds ρ_a by $\sim 10\times$, accuracy drops. Row 3: τ exceeds ρ_a by $\sim 100\times$, learning is erased. The ρ_a -controller (gold) survives all spikes.

tending the spike test to broader architectures, we compare the ρ_a -controller against plain Adam and gradient clipping ($\|g\| \leq 1$). Figure 10 tests three methods across three architectures and four spike severities. As the spike magnitude increases, plain Adam (red) fails progressively: the Transformer recovers from $10\times$ but not $1000\times$; MLP with LayerNorm (MLP+LN) tolerates $100\times$ but collapses at $10000\times$; a convolutional network with BatchNorm (CNN+BN) shows permanent collapse even at $10\times$ because BatchNorm’s running statistics become corrupted.

Gradient clipping (teal, threshold 1) provides partial protection—it improves on plain Adam at moderate spikes—but it applies a uniform norm threshold that does not adapt to the local radius ρ_a . At $10000\times$, clipping still leaves Transformer and CNN+BN in high-loss states. The ρ_a -controller (gold) survives all conditions by capping $\tau \leq \rho_a$.

Table 1. Median final test accuracy at $10000\times$ spike. A seed is divergent if final loss exceeds 10.

Arch	Plain	Clip	ρ_a -ctrl
Transformer	31.8%	38.7%	95.3%
MLP+LN	44.6%	51.5%	93.9%
CNN+BN	13.4%	10.3%	71.6%

Table 1 quantifies the $10000\times$ column. Gradient clipping improves MLP+LN to 51.5% but still falls far short of the 93.9% reached by the ρ_a -controller. For Transformer and CNN+BN, clipping fails entirely. The geometric difference is the key: clipping imposes a fixed norm threshold, whereas the ρ_a -controller scales the update against the local radius. When the safe radius contracts unevenly, a fixed threshold can still permit $r > 1$.

Phase Transition via JVP-Based ρ_a : Linear Model at $r = 1$

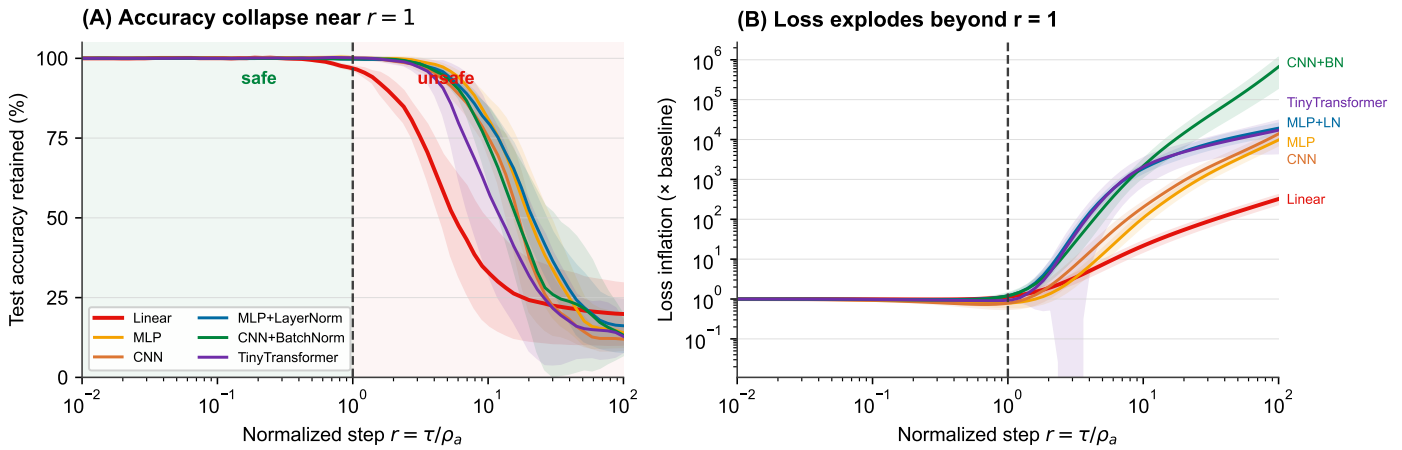


Figure 7. Phase transition across architectures. Six architectures trained to convergence, then one gradient step at varying r . (A) Test accuracy retained. Linear model transitions at $r \approx 1$. Other architectures retain confidence-margin slack. (B) Loss inflation (post-step loss / pre-step loss).

Transition near $r=1$ validates the analyticity radius as stability boundary

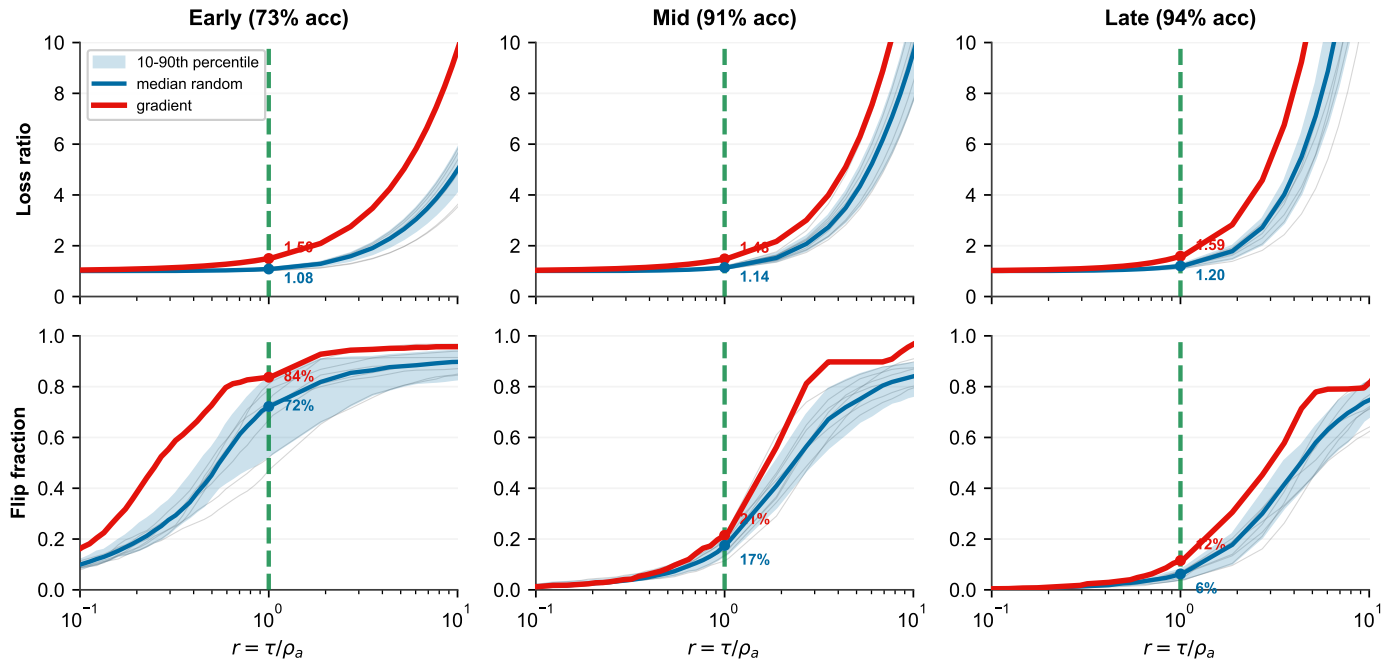


Figure 8. Random-direction sweeps. Both loss ratio and flip fraction transition near $r \approx 1$ across all tested phases, supporting r as direction-independent in these settings.

6.6 Transformer Layer Analysis

The preceding experiments used a single output-logit radius. The checked-in transformer artifact behind Figure 11 compares four strategies on a tiny transformer ($d = 32$, 2 layers) trained on the Digits dataset: two adaptive controllers and two fixed learning rates, with the highest fixed rate set to $16\times$ the lowest. In that artifact, the all-radii controller uses three local radii:

- $\rho_{\text{out}} = \pi/\Delta_{\text{out}}$: output logit spread (same as Section 4).
- $\rho_{\text{attn}} = \pi/\Delta_{\text{attn}}$: pre-softmax attention-logit spread (minimum across heads).
- $\rho_{\text{ffn}} = Q_{0.01}(|h|/|\dot{h}|)$: a conservative FFN kink-distance proxy, defined as the 1% quantile of $|h|/|\dot{h}|$ over FFN preactivations. This is the only included experiment that augments the softmax radii with a non-softmax term; see Section Appendix 2.

Temperature Fingerprint: Multi-seed Median+IQR

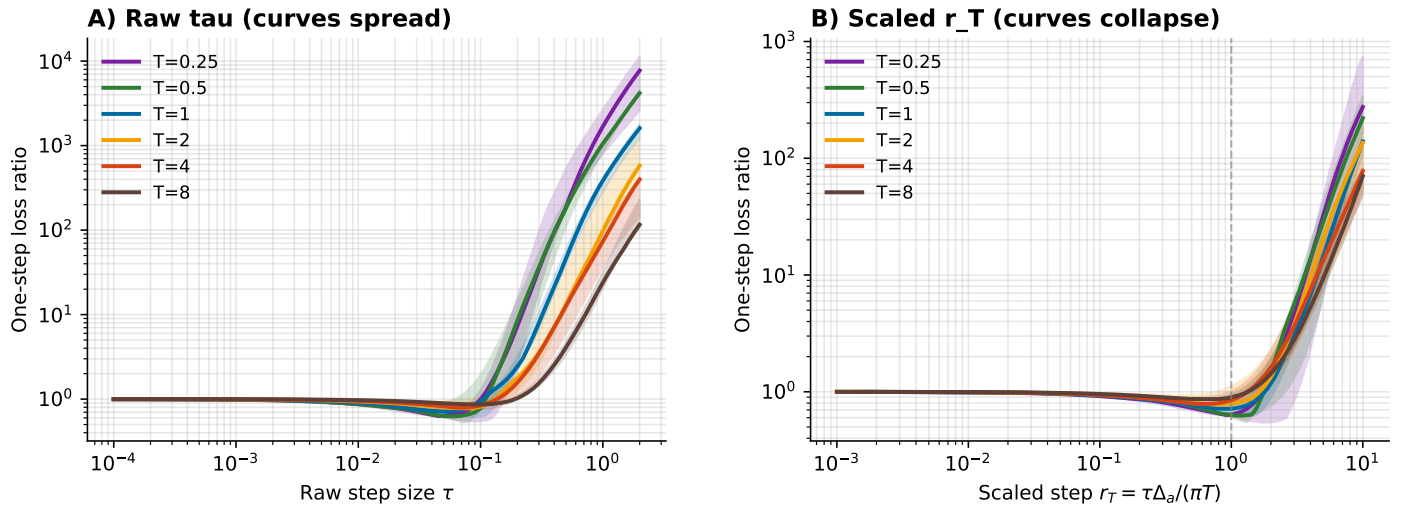


Figure 9. Temperature-scaling fingerprint test. One-step loss inflation (post-step loss / pre-step loss) is measured across temperatures $T \in \{0.25, 0.5, 1, 2, 4, 8, 16, 64\}$. **A:** plotted against raw step size τ , collapse thresholds vary substantially across T (collapse std = 0.992). **B:** plotted against the theory-normalized coordinate $r_T = \tau\Delta_a/(\pi T) = \tau/\rho_a(T)$, curves align much more tightly (collapse std = 0.164).

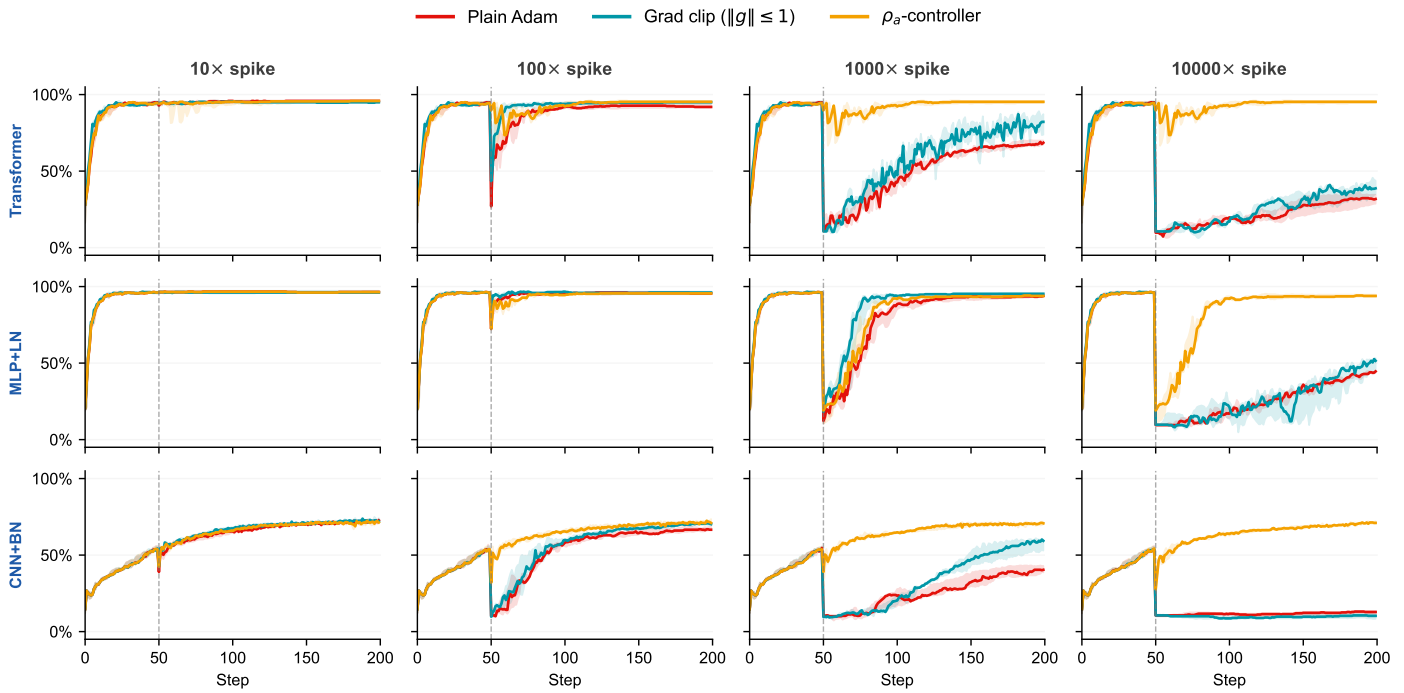


Figure 10. Controller across architectures and spike severities (5 seeds, median with IQR bands). Each column increases the spike magnitude from $10\times$ to $10000\times$. Red: plain Adam. Teal: Adam with gradient clipping ($\|g\| \leq 1$). Gold: ρ_a -controller. Gradient clipping helps partially at moderate spikes but still collapses at high severity. The ρ_a -controller survives all conditions.

The network radius is $\rho_{\text{net}} = \min(\rho_{\text{out}}, \rho_{\text{attn}}, \rho_{\text{ffn}})$ for the all-radii controller, while the output-only controller uses only ρ_{out} .

The right panel shows that the effective learning rate allowed by the convergence-radius bound changes by orders of magnitude throughout training and oscillates unpredictably. No fixed schedule can track this variation.

A rate that works at step 50 may violate the bound by step 150—heuristics work until they fail.

The left panel shows the consequence. Fixed learning rates face an impossible tradeoff: $1\times$ converges slowly, while $16\times$ diverges. The adaptive controllers avoid this tradeoff by tracking the local radius. Remarkably, the most conservative strategy ($\min(\rho_{\text{out}}, \rho_{\text{attn}}, \rho_{\text{ffn}})$) reaches the

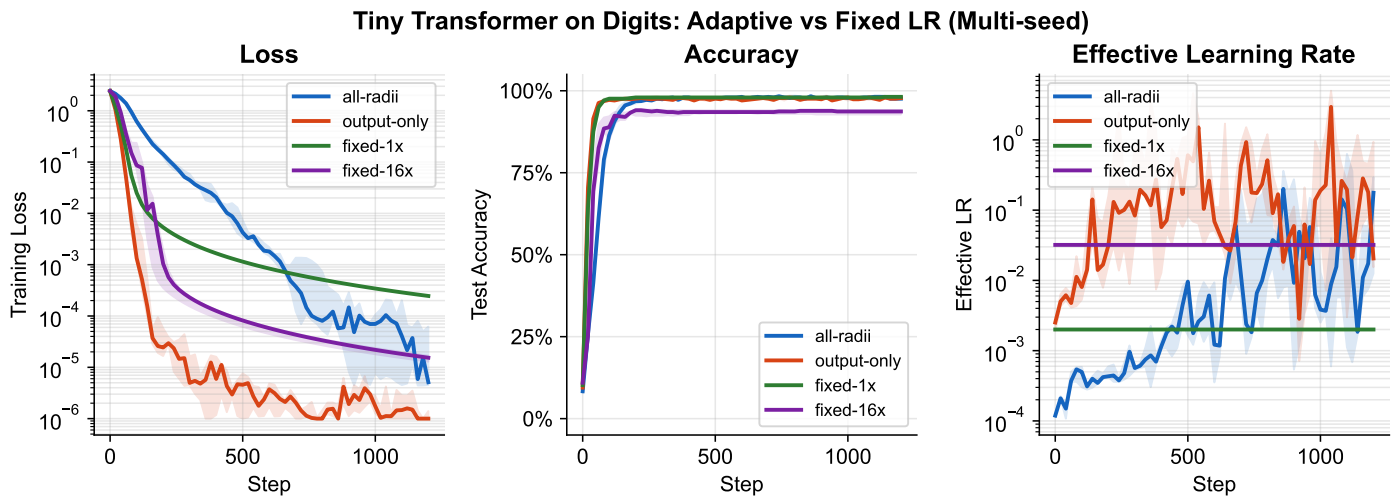


Figure 11. Tiny transformer on Digits: adaptive vs fixed learning rates (5 seeds, median with IQR bands). Left: training loss. Center: test accuracy. Right: effective LR. The adaptive controllers (all-radii, output-only) vary their step size by orders of magnitude throughout training. Fixed LRs either converge slowly (1 \times) or diverge (16 \times). The most conservative strategy (all-radii, using $\min(\rho_{\text{out}}, \rho_{\text{attn}}, \rho_{\text{ffn}})$) reaches the lowest loss and highest accuracy.

Table 2. Which radius binds in the all-radii transformer run (Figure 11; 5 seeds, 61 logged evaluations per seed). Counts report how often each term attained $\rho_{\text{net}} = \min(\rho_{\text{out}}, \rho_{\text{attn}}, \rho_{\text{ffn}})$ within each training phase. Median radii are pooled over all logged points in that phase.

Phase	FFN	Out	Attn	med. ffn	med. out	med. attn
Early	94/100	6/100	0/100	0.0164	0.0307	0.645
Middle	48/100	52/100	0/100	0.0111	0.0107	0.203
Late	8/105	97/105	0/105	0.0131	0.00793	0.168

lowest loss. Conservative steps compound; aggressive steps erase progress.

Table 2 shows that the bottleneck pattern in this artifact is not attention-first. Across all 5 seeds and 61 logged evaluations per seed, ρ_{attn} never attains the minimum. Early training is FFN-limited, the middle third mixes FFN and output bottlenecks, and late training is overwhelmingly output-limited. Every seed starts FFN-limited and ends output-limited. So the observed transition in this artifact is FFN early \rightarrow output late.

6.7 Natural Instability Detection

The preceding experiments validate r through artificial perturbations: injected LR spikes, single-step sweeps, and controlled temperature shifts. A natural question is whether r also tracks instabilities that arise organically during standard training—without any injected spike.

Figure 12 tests this on a larger-scale setting: ResNet-18 trained from scratch on CIFAR-10 with SGD and momentum 0.9. Four learning rates span from conservative ($\eta = 0.005$) to aggressive ($\eta = 0.5$), with $r = \tau/\rho_a$ logged every 50 steps using a finite-difference estimate of

ρ_a on a current-batch subset (up to 256 samples). The step size $\tau = \eta \|v\|$ uses the full momentum-corrected update vector v , not the raw gradient, and we train for 10 epochs to focus on the r -accuracy correlation (longer runs remain future work; Section 8).

The results separate cleanly by r . At $\eta = 0.005$, the ratio stays near 1 and median final accuracy is 80.4%. At $\eta = 0.01$, occasional violations appear and accuracy reaches 82.6%. At $\eta = 0.1$, violations are frequent and accuracy drops to 78.5%. At $\eta = 0.5$, the run sits deep in the $r > 1$ regime and degrades to 57.5%. Notably, even $\eta = 0.005$ exceeds $r=1$ once due to momentum amplification—no fixed LR is unconditionally safe. Can the controller do better?

Four ρ_a -controller targets confirm the bound’s role. Crucially, the controller uses no base learning rate: it sets $\eta = r \rho_a / \|v\|$ from the local geometry and the chosen target r , replacing a base-LR choice with a dimensionless aggressiveness target. At $r=1$, the controller reaches the highest accuracy (85.3%), exceeding every fixed LR. At $r=0.5$ (conservative), it matches the best fixed rate (80.4%). At $r=2$, accuracy remains strong (84.4%), consistent with the confidence-margin slack observed in the single-step experiments. At $r=4$, accuracy drops to 72.1% with large seed-to-seed variance (IQR 38.9–74.2%), confirming that sufficiently exceeding the bound is genuinely harmful.

Three aspects strengthen this result. First, no perturbation was injected—the instabilities emerge from the natural interaction of learning rate, gradient magnitude, and local loss geometry. Second, the optimizer is SGD rather than Adam, so the same qualitative pattern appears outside the Adam-based spike tests. Third, the shrinking-

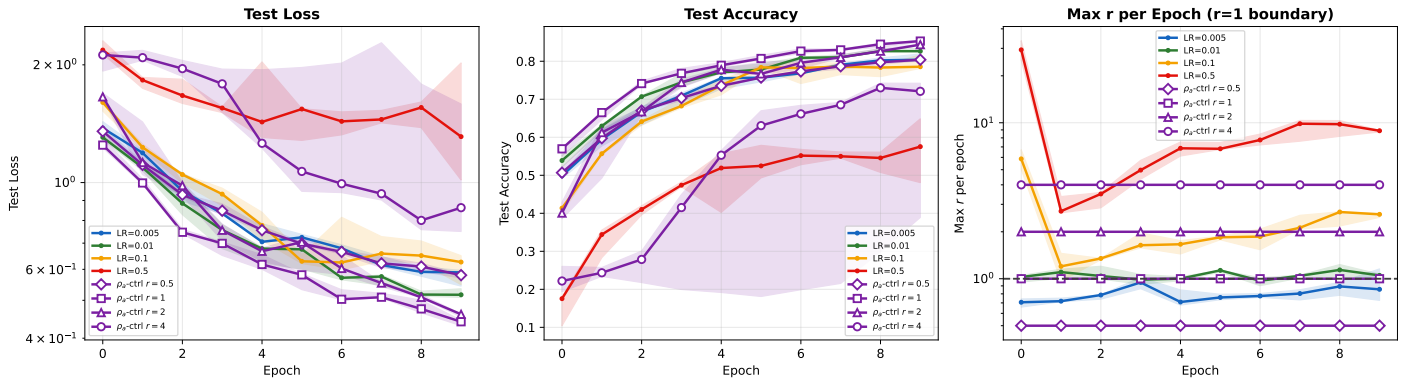


Figure 12. Natural instability detection: ResNet-18 on CIFAR-10 with SGD+momentum at four fixed learning rates and four ρ_a -controller targets ($r=0.5, 1, 2, 4$; 5 seeds, median with IQR bands). **Left:** test loss. **Center:** test accuracy. **Right:** maximum $r = \tau/\rho_a$ per epoch with the $r=1$ boundary (dashed). Step size τ includes the momentum buffer. The controller at $r=1$ reaches the highest accuracy (85.3%); $r=2$ remains stable; $r=4$ degrades with high variance. Even $\eta=0.005$ occasionally exceeds $r=1$ due to momentum.

Table 3. ResNet-18 CIFAR-10 natural instability summary (5 seeds, 10 epochs, momentum-corrected τ). The controller at $r=1$ is optimal; $r=2$ retains accuracy from confidence-margin slack; $r=4$ degrades. Even $\eta=0.005$ exceeds $r=1$ due to momentum.

Method	max r	$r > 1$	Acc (med.)	IQR
$\eta=0.005$	1.11	1	80.4%	80.0–81.9%
$\eta=0.01$	1.23	13	82.6%	82.6–83.4%
$\eta=0.1$	5.87	58	78.5%	78.1–81.7%
$\eta=0.5$	29.34	70	57.5%	48.1–64.8%
ρ_a -ctrl ($r=0.5$)	0.50	0	80.4%	80.2–80.5%
ρ_a -ctrl ($r=1$)	1.00	0 [†]	85.3%	85.1–85.4%
ρ_a -ctrl ($r=2$)	2.00	80	84.4%	84.3–84.5%
ρ_a -ctrl ($r=4$)	4.00	80	72.1%	38.9–74.2%

[†] Strict exceedances are machine-precision noise only ($< 10^{-15}$).

radius story still appears: as training sharpens predictions, ρ_a contracts and aggressive fixed learning rates move into progressively higher- r regimes later in training. Table 3 quantifies the separation.

No fixed rate keeps r below 1 throughout training once momentum is accounted for. As violations accumulate, accuracy degrades monotonically. The controller results bracket the bound: $r=1$ is optimal, $r=2$ retains accuracy from confidence-margin slack, and $r=4$ collapses.

Summary. The normalized step size $r = \tau/\rho_a$ reliably predicts instability in our tested architectures and directions: $r < 1$ remained safe throughout these experiments. The bound generalizes across architectures (six tested), directions (gradient and 20 random), and optimizers (Adam and SGD), and temperature normalization collapses onset thresholds with a $6\times$ reduction in spread. Beyond controlled perturbations, r tracks instability in natural ResNet-18/CIFAR-10 training without any injected spike, and

controller targets that bracket the bound ($r=0.5, 1, 2, 4$) show that $r=1$ is optimal while degradation sets in beyond $r=2$. The bound is conservative—most models survive to $r > 1$ —but that conservatism is explained by confidence-margin slack. Exploiting this bound, the ρ_a -controller survives adversarial LR spikes up to 10,000 \times , including regimes where gradient clipping collapses.

7. Related Work

We connect several strands of optimization and deep-learning theory through a single quantity: the **computable convergence-radius bound** ρ_a . Each strand captures part of why training fails, but none identifies a common mechanism or explains why instabilities erupt on apparently smooth landscapes. The convergence-radius bound serves as both a theoretical lens and a cheap diagnostic.

Stability and curvature. Cohen et al. [9] observe the *edge of stability*: gradient descent keeps $\lambda_{\max}(H) \approx 2/\eta$. Gilmer et al. [10] link curvature spikes to instability but use empirical sharpness rather than the underlying analytic structure. Classic theory demands global L -smoothness ($\eta < 2/L$) or local variants [4] that scale L with the gradient norm. These bounds control the quadratic approximation error. The convergence radius controls the entire Taylor series rather than only its quadratic error. That shifts the question from “how wrong is the local model?” to “does the series converge at all at the proposed step?”

Step-size control. Natural-gradient methods [11] and trust-region updates use Fisher information or KL divergence to stay inside reliable regions; the convergence-radius bound formalizes a similar idea in function space at

the cost of one JVP. Adam [12] and gradient clipping [4, 3] treat the *symptoms* of instability without exposing the cause. Classical rules such as Polyak’s method [13] and Armijo line search [14] adapt step length through objective values or sufficient-decrease tests on \mathbb{R} . Our controller differs in mechanism: it estimates distance to a complex singularity before the step, so the governing variable is not a descent test on \mathbb{R} but the analyticity boundary itself.

Scaling and parameterization. Maximal update parametrization (μ P) and μ Transfer [15] aim to preserve useful hyperparameters across width and model scale. That is complementary rather than competing with our goal. μ P addresses how to transfer hyperparameters across a family of models; ρ_a measures local step safety within one fixed model and training run.

Empirical training dynamics. Chowdhery et al. [1] report sudden loss spikes during PaLM training; Touvron et al. [2] document similar shocks in LLaMA training. Our interpretation is that these reflect steps that exceed a shrinking ρ_a . Lewkowycz et al.’s “catapult phase” [16]—a brief divergence followed by convergence to flatter minima—is consistent with r moderately above 1 in our experiments. Very large r values are much more likely to collapse runs.

Softmax and cross-entropy dynamics. Agarwala et al. [17] show that early learning under softmax cross-entropy is governed by inverse temperature and initial logit scale. Balduzzi et al. [18] analyze optimization in rectifier networks through neural Taylor approximations. Haas et al. [19] identify a “controlled divergence” regime: under cross-entropy, logits can grow unboundedly while loss, gradients, and activations remain stable. Our framework offers a mechanism for this phenomenon—partition zeros sit at fixed imaginary distance π regardless of logit magnitude, so the loss surface appears smooth on \mathbb{R} even as the convergence radius shrinks. To our knowledge, none of these works use the distance to complex partition zeros as a step-size variable.

Theoretical foundations. The step-size limit stems from classical bounds on zeros of exponential sums $\sum w_k e^{a_k t}$. The Lee–Yang theorem [20] and extensions by Ruelle [21], Turán [22], and Moreno [23] locate such zeros. In numerical linear algebra, Sao [24] showed that convergence-radius constraints on moment-generating functions cap trace-power estimators for log-determinants. We transfer this insight to optimization: the partition function $F(\tau) = \sum w_k e^{a_k \tau}$ underlying cross-entropy has complex

zeros, and those zeros set the Taylor convergence radius and hence the safe step size.

Singular learning theory. Watanabe’s singular learning theory [25, 26] and related work [27] use zeta functions and analytic continuation to characterize model complexity via poles of a learning coefficient (the real log-canonical threshold). This shares our language of singularities and analytic continuation but addresses a different question: generalization and model selection, not optimizer step control. Their singularities are algebraic—poles of a zeta function encoding parameter-space geometry. Ours are transcendental—zeros of the partition function $F(\tau)$ in the complex step-parameter plane.

Singularity-aware step control. The closest precedent lies outside machine learning, in numerical continuation methods. Verschelde and Viswanathan [28] use Fabry’s ratio theorem as a “radar” to detect nearby complex singularities and adapt step size in homotopy path tracking. Telen et al. [29] use Padé approximants for the same purpose: locate the nearest singularity and set the trust region accordingly. Timme [30] builds path-tracking controllers that exploit distance to the closest singularity for precision and step-size decisions. Our work transfers this principle—measure singularity distance, bound the step—from polynomial system solving to neural network optimization, with partition-function zeros of cross-entropy as the relevant singularities.

Continual learning. Elastic Weight Consolidation [31] and natural-gradient methods [11] guard prior knowledge with Fisher-based importance. The convergence-radius bound offers a function-space view: learned logits create singularities that shrink the region of reliable updates. The scalar $\rho_a = \pi/\Delta_a$ —one JVP—measures the remaining headroom for safe learning.

8. Discussion and Conclusion

8.1 Summary

We showed that cross-entropy loss carries a geometric constraint that standard smoothness analysis does not capture: complex singularities of the partition function cap the Taylor convergence radius along every update direction. Under linearized logits—a tractability choice that makes the constraint both computable and interpretable—the radius yields the bound $\rho_a = \pi/\Delta_a$ (one Jacobian–vector product). For binary cross-entropy the exact radius is $\rho^* = \sqrt{\delta^2 + \pi^2}/\Delta_a$; the bound ρ_a is the worst case ($\delta = 0$) and applies to n classes. The bound is conservative: no

tested architecture failed below it, but some survive above it. As training sharpens predictions, Δ_a grows and the bound tightens—explaining why late-training updates become fragile even as the loss surface appears flatter on \mathbb{R} .

This bound has a simple interpretation. The loss landscape remains smooth on \mathbb{R} , but beyond the convergence radius the Taylor series diverges, so adding more terms worsens the approximation rather than improving it. Step-size guarantees that rely on local polynomial extrapolation therefore lose predictive power beyond ρ_a . Standard L -smoothness descent lemmas remain valid under their own assumptions but do not encode this singularity geometry— ρ_a captures a separate, often stricter, constraint.

8.2 Interpretation

Single-step hazard vs multi-step dynamics. Our bounds describe one-step reliability. They quantify local hazard, not full training dynamics. A run can survive occasional high-hazard updates if the iteration is self-correcting; however, repeated high-hazard updates can accumulate through feedback and destabilize training. This distinction matters for interpretation: r is a risk scale, while long-run divergence depends on how r interacts with data conflict, architectural slack, and optimizer dynamics.

Global controls vs local stability. Temperature and learning-rate schedules both act as indirect global controls, while instability is governed by the local normalized step $r = \tau/\rho_a$. When control targets the wrong variable (raw τ or a fixed global T), updates can still violate $r > 1$ on hard batches or directions. The temperature-fingerprint experiment (Section 6) confirms this: a fixed T provides no per-batch safety guarantee, but normalization by ρ_a collapses onset thresholds across temperatures.

8.3 Why One-Step Metrics Matter for Instability

The one-step metrics we report (loss inflation, retained accuracy, and flip fraction) directly measure whether an update preserved or damaged local model reliability. Although these metrics capture single-step behavior, they matter for iterative training because each update sets the next model state and the next gradient. Large one-step disruptions can produce decision-boundary churn that amplifies over subsequent updates.

This is why the transition near $r \approx 1$ is important: it provides a practical operating boundary. We do not claim that $r > 1$ always causes divergence. Rather, crossing this boundary makes harmful one-step events more likely, which increases instability risk when feedback dynamics are unfavorable.

Beyond Convergence Radius, Hessian Overestimates Safe Step Exponentially

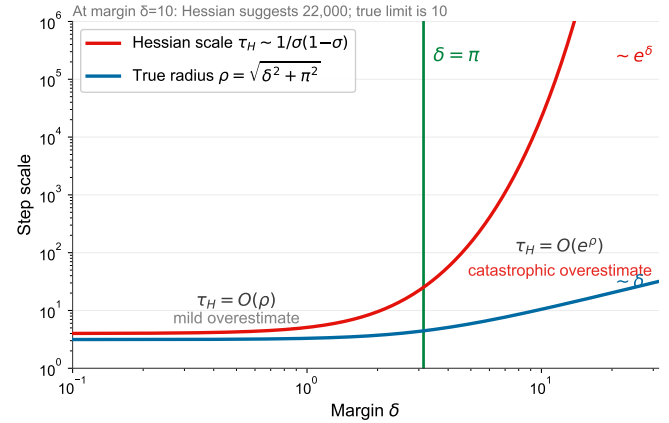


Figure 13. Hessian curvature $\sigma(1 - \sigma) \sim e^{-\delta}$ vanishes exponentially while the radius bound $\pi/\sqrt{\delta^2 + \pi^2}$ decays only algebraically. At $\delta = 10$, the mismatch exceeds 4000 \times .

Together, these two levels connect theory and practice: ρ_a provides a computable local reliability scale, while one-step metrics show the observable consequences of violating that scale.

8.4 Why Training Tightens the Bound

During training, the model separates logits to sharpen predictions, causing Δ_a to grow. Since $\rho_a = \pi/\Delta_a$, the safe radius shrinks. A learning rate that met $r < 1$ early in training may violate this condition later.

Concretely, $\rho_a \approx 3.14$ when $\Delta_a = 1$, drops to 0.31 when $\Delta_a = 10$, and to 0.10 when $\Delta_a = 30$. With a fixed $\eta = 0.01$ and $\|\nabla f\| = 10$, the step $\tau = 0.1$ gives $r = 0.03$ early but $r = 1.0$ later.

Rather than arbitrary “cooling down,” learning rate decay tracks the contracting safe region. Warmup serves the opposite role. Early in training, Δ_a is small (logits are similar), so ρ_a is large. However, step norms $\|p\|$ can also be large. Warmup caps η to prevent $\tau = \|p\|$ from exceeding this generous radius before updates stabilize.

8.5 Hessian Intuition Versus Radius Geometry

Figure 13 is best read as an interpretation of the binary theory, not as a separate empirical result. For scalar logistic loss at margin δ , Hessian curvature decays like $\sigma(\delta)(1 - \sigma(\delta)) \sim e^{-\delta}$, while the exact binary convergence radius from Theorem 4.3 scales only like $\sqrt{\delta^2 + \pi^2} \sim \delta$. So a curvature-only view says confident examples become flatter and therefore safer, whereas the radius view says Taylor reliability can still tighten because the relevant complex singularities remain at imaginary distance π .

This resolves the apparent paradox from training practice: the loss surface can look flatter on \mathbb{R} even as updates

become more fragile. Flatness on the real line and distance to complex singularities are different notions of safety, and cross-entropy forces them apart.

8.6 Limitations

Linearization. Linearization is a tractability choice, not the source of the phenomenon. The true loss $\ell(\tau)$ has a convergence radius set by its own complex singularities regardless of how logits depend on τ . Linearization yields the closed-form bound $\rho_a = \pi/\Delta_a$ and reveals the controlling variable; for deep networks where logits curve over the step, the true radius may be larger or smaller than this estimate. Empirical validation (Section 6) shows that the linearized bound remains predictive in the tested settings.

Scale of validation. Our motivating examples come from frontier-scale training. As is standard for mechanism-identification work, the direct evidence here uses controlled small-scale systems (plus ResNet-18/CIFAR-10 and a tiny transformer) where variables can be isolated. Testing the diagnostics at frontier scale is an immediate next step.

Bound vs exact. The lower bound $\rho_a = \pi/\Delta_a$ is conservative by construction—it is the worst-case (balanced-logit) specialization of the exact binary radius. Conservativeness is expected: a lower bound on a convergence radius should not over-promise safety. Tightening the bound via the sample-specific logit gap δ is a natural refinement.

Overhead. On ResNet-18/CIFAR-10 (batch 128, RTX 6000 Ada), a baseline SGD+momentum step (forward + backward + optimizer) takes 12.6 ms. Finite-difference ρ_a estimation raises this to 20.9 ms (+66%); exact JVP to 28.7 ms (+129%). Finite differences are approximate but cheaper; JVP is exact. These numbers are for ResNet-18 only; overhead on large-scale models remains to be measured.

Multi-step dynamics. The radius bounds single-step reliability, not training trajectories. Intermittent $r > 1$ can cause loss oscillations that self-correct; divergence in our experiments required $r > 1$ consistently over several iterations (Section 8.2). Whether a run survives depends on data quality, architecture, optimizer momentum, and schedule—variables beyond the one-step geometry.

Generalization. The Taylor radius constrains local update reliability, not what the model learns. It does not, by itself, prevent overfitting or predict generalization. These depend on data quality, regularization, and architecture choices that the radius does not capture.

Scope. This paper focuses on softmax singularities: output logits and attention pre-softmax scores. Activation functions and normalization layers introduce additional singularities (Section Appendix 2), which can become the bottleneck in unnormalized networks. We do not systematically test activation-function singularities, though the checked-in tiny-transformer artifact includes a conservative FFN kink proxy $\rho_{\text{ffn}} = Q_{0.01}(|h|/|h|)$ from Section Appendix 2 as a single data point. That experiment is FFN-limited early and output-limited late, while the attention-softmax radius never binds. All experiments use small models (up to 128 dimensions); validation on large-scale production transformers is still needed.

Computation. We provide preliminary overhead numbers for computing ρ_a via JVP and finite differences; optimizing this computation is not the focus. The bound should be computed over all training samples, but this can be expensive; mini-batch estimates are practical but approximate.

Higher-order extensions. Linearization is not the only possible proxy. Quadratic, cubic, or Padé logit models can refine the estimate (requiring Hessian-vector products), but the linearized model is already valuable: it gives a closed-form mechanism, a cheap diagnostic, and the right controlling variable Δ_a . The underlying principle—that complex zeros determine the radius—does not change.

Controller. The ρ_a -controller demonstrates that the bound is actionable, not merely diagnostic. Integrating it with Adam’s momentum, modern schedulers, and production-scale workloads are natural engineering extensions.

8.7 Takeaways

The central finding is that cross-entropy training operates under a convergence-radius constraint set by complex singularities of the loss—a constraint invisible to standard real-variable smoothness analysis. Three practical consequences follow:

1. **Diagnosis.** If training diverges, compute $r = \|p\|/\rho_a$ at that step, where p is the optimizer update and ρ_a uses a JVP along $p/\|p\|$. If $r > 1$, the instability was predictable from the analytic structure.
2. **Monitoring.** Track $\rho_a = \pi/\Delta_a$ during training. This requires one JVP per step, costing about as much as a forward pass. A shrinking ρ_a signals that the current learning rate may become unsafe; decay it preemptively.
3. **Adaptive control.** Cap $\tau \leq \rho_a$ to guarantee $r \leq 1$. This reduces sensitivity to the learning rate: a wide range

of learning rates can be made safe by capping with the radius.

The bound is conservative—models often survive $r > 1$ —but no architecture in our small-scale experiments failed below it. Large-scale validation is needed before production use. The deeper point is structural: the geometric constraint is intrinsic to cross-entropy and does not disappear with better optimization. The ghosts are always there; the question is whether the step reaches them.

8.8 Future Work

The most immediate next step is large-scale validation on models such as Pythia and OLMo. We could also integrate our method with Adam, using ρ_a to modulate the step size after momentum and second-moment scaling. Alternatively, regularization that penalizes large Δ_a could maintain a larger bound and offer an alternative to post-hoc learning-rate reduction.

References

- [1] Aakanksha Chowdhery et al. “PaLM: Scaling language modeling with Pathways”. In: *Journal of Machine Learning Research* 24.240 (2023), pp. 1–113.
- [2] Hugo Touvron et al. “LLaMA: Open and efficient foundation language models”. In: *arXiv preprint arXiv:2302.13971* (2023).
- [3] Razvan Pascanu, Tomas Mikolov, and Yoshua Bengio. “On the difficulty of training recurrent neural networks”. In: *International Conference on Machine Learning* (2013), pp. 1310–1318.
- [4] Jingzhao Zhang et al. “Why gradient clipping accelerates training: A theoretical justification for adaptivity”. In: *International Conference on Learning Representations*. 2020.
- [5] Ilya Loshchilov and Frank Hutter. “SGDR: Stochastic gradient descent with warm restarts”. In: *International Conference on Learning Representations*. 2017.
- [6] Christian Szegedy et al. “Rethinking the inception architecture for computer vision”. In: *IEEE Conference on Computer Vision and Pattern Recognition*. 2016, pp. 2818–2826.
- [7] Gabriel Pereyra et al. “Regularizing neural networks by penalizing confident output distributions”. In: *arXiv preprint arXiv:1701.06548* (2017).
- [8] John B Conway. *Functions of One Complex Variable I*. Springer, 1978.
- [9] Jeremy M Cohen et al. “Gradient descent on neural networks typically occurs at the edge of stability”. In: *International Conference on Learning Representations*. 2021.
- [10] Justin Gilmer et al. “A loss curvature perspective on training instabilities of deep learning models”. In: *International Conference on Learning Representations* (2022).
- [11] Shun-ichi Amari. “Natural gradient works efficiently in learning”. In: *Neural Computation* 10.2 (1998), pp. 251–276.
- [12] Diederik P Kingma and Jimmy Ba. “Adam: A method for stochastic optimization”. In: *International Conference on Learning Representations* (2015).
- [13] B. T. Polyak. “Some methods of speeding up the convergence of iteration methods”. In: *U.S.S.R. Computational Mathematics and Mathematical Physics* 4.5 (1964), pp. 1–17. doi: [10.1016/0041-5553\(64\)90137-5](https://doi.org/10.1016/0041-5553(64)90137-5).
- [14] Larry Armijo. “Minimization of functions having Lipschitz continuous first partial derivatives”. In: *Pacific Journal of Mathematics* 16.1 (1966), pp. 1–3. doi: [10.2140/pjm.1966.16.1](https://doi.org/10.2140/pjm.1966.16.1).
- [15] Greg Yang et al. *Tensor Programs V: Tuning Large Neural Networks via Zero-Shot Hyperparameter Transfer*. 2022. arXiv: [2203.03466](https://arxiv.org/abs/2203.03466) [cs.LG].
- [16] Aitor Lewkowycz et al. “The large learning rate phase of deep learning: the catapult mechanism”. In: *arXiv preprint arXiv:2003.02218* (2020).
- [17] Atish Agarwala et al. *Temperature check: theory and practice for training models with softmax-cross-entropy losses*. 2020. arXiv: [2010.07344](https://arxiv.org/abs/2010.07344) [cs.LG].
- [18] David Balduzzi, Brian McWilliams, and Tony Butler-Yeoman. “Neural Taylor approximations: convergence and exploration in rectifier networks”. In: *International Conference on Machine Learning*. Vol. 70. Proceedings of Machine Learning Research. PMLR, 2017, pp. 351–360.
- [19] Moritz Haas et al. *On the surprising effectiveness of large learning rates under standard width scaling*. 2025. arXiv: [2505.22491](https://arxiv.org/abs/2505.22491) [cs.LG].
- [20] T D Lee and C N Yang. “Statistical theory of equations of state and phase transitions. II. Lattice gas and Ising model”. In: *Physical Review* 87.3 (1952), pp. 410–419.
- [21] David Ruelle. “Extension of the Lee–Yang circle theorem”. In: *Physical Review Letters* 26.6 (1971), pp. 303–304.
- [22] Pál Turán. *Eine neue Methode in der Analysis und deren Anwendungen*. Akadémiai Kiadó, Budapest, 1953.
- [23] Carlos Julio Moreno. “On the zeros of exponential polynomials”. In: *Journal of Mathematical Analysis and Applications* 44.2 (1973), pp. 418–426.
- [24] Piyush Sao. “What trace powers reveal about log-determinants: closed-form estimators, certificates, and failure modes”. In: *arXiv preprint arXiv:2601.12612* (2026).
- [25] Sumio Watanabe. “Asymptotic equivalence of Bayes cross validation and widely applicable information criterion in singular learning theory”. In: *Journal of Machine Learning Research* 11 (2010), pp. 3571–3594.
- [26] Sumio Watanabe. “A widely applicable Bayesian information criterion”. In: *Journal of Machine Learning Research* 14.Mar (2013), pp. 867–897.
- [27] Koshi Yamada and Sumio Watanabe. *Statistical learning theory of quasi-regular cases*. 2011. arXiv: [1111.1832](https://arxiv.org/abs/1111.1832) [math.ST].
- [28] Jan Verschelde and Kylash Viswanathan. *Locating the closest singularity in a polynomial homotopy*. 2022. arXiv: [2205.07380](https://arxiv.org/abs/2205.07380) [math.NA].
- [29] Simon Telen, Marc Van Barel, and Jan Verschelde. “A robust numerical path tracking algorithm for polynomial homotopy continuation”. In: *SIAM Journal on Scientific Computing* 42.6 (2020), A3637–A3657. doi: [10.1137/19M1288036](https://doi.org/10.1137/19M1288036).
- [30] Sascha Timme. “Mixed precision path tracking for polynomial homotopy continuation”. In: *Advances in Computational Mathematics* 47.5 (2021), p. 75. doi: [10.1007/s10444-021-09899-y](https://doi.org/10.1007/s10444-021-09899-y).

- [31] James Kirkpatrick et al. “Overcoming catastrophic forgetting in neural networks”. In: *Proceedings of the National Academy of Sciences* 114.13 (2017), pp. 3521–3526.
- [32] Eugène Rouché. *Mémoire sur la série de Lagrange*. Vol. 22. See also Conway (1978), Theorem VI.1.2. 1862, pp. 193–224.
- [33] Stefan Elfving, Eiji Uchibe, and Kenji Doya. “Sigmoid-weighted linear units for neural network function approximation in reinforcement learning”. In: *Neural Networks* 107 (2018), pp. 3–11.
- [34] Noam Shazeer. “GLU Variants Improve Transformer”. In: *arXiv preprint arXiv:2002.05202*. 2020.
- [35] Dan Hendrycks and Kevin Gimpel. “Gaussian Error Linear Units (GELUs)”. In: *arXiv preprint arXiv:1606.08415* (2016).
- [36] Tiberiu Popoviciu. “Sur les équations algébriques ayant toutes leurs racines réelles”. In: *Mathematica (Cluj)* 9 (1935), pp. 129–145.

Appendix 1. From Linearized Theory to Real Networks

The true loss $\ell(\tau)$ has its own convergence radius, set by its nearest complex singularity. The linearized-logit model is useful because it yields a closed-form softmax lower bound and makes the governing quantity Δ_a explicit. This appendix studies when that first-order proxy remains reliable in deeper nonlinear networks.

Appendix 1.1 From the True Radius to a Tractable Proxy

The key approximation replaces the true (nonlinear) logit trajectories $z_i(\tau) = z_i(\theta + \tau\nu)$ with their linearizations $z_i(0) + a_i\tau$. This is exact when only the output layer moves; for deeper layers it introduces error depending on logit curvature.

The true univariate loss $\ell(\tau) = f(\theta + \tau\nu)$ has logits that are nonlinear functions of τ . Writing $z_i(\tau) = z_i(0) + a_i\tau + r_i(\tau)$ where $|r_i(\tau)| \leq C_i|\tau|^2/2$ and C_i captures the logit Hessian along ν , the linearized exponential sum $F_{\text{lin}}(\tau) = \sum w_i e^{a_i\tau}$ is perturbed to $F_{\text{true}}(\tau) = \sum e^{z_i(\tau)}$.

Appendix 1.1.1 When linearization is exact

If the output layer is linear ($z = Wh + b$) and only output-layer parameters move, then $z_i(\tau)$ is exactly linear in τ . In this case, ρ^* is the true radius. For deeper layers, the composition of nonlinear activations makes $C_i > 0$.

Appendix 1.1.2 Perturbation of zeros

The linearized F_{lin} has zeros at imaginary distance π/Δ_a from the origin (Theorem 4.6). We can bound how far these zeros shift under the nonlinear perturbation. Factor F_{true} as:

$$F_{\text{true}}(\tau) = F_{\text{lin}}(\tau) \cdot \left(1 + \frac{F_{\text{true}}(\tau) - F_{\text{lin}}(\tau)}{F_{\text{lin}}(\tau)}\right) \quad (20)$$

For $|\tau| \leq \pi/\Delta_a$, each remainder satisfies $|r_i(\tau)| \leq C\pi^2/(2\Delta_a^2)$ where $C = \max_i C_i$. Define the conservative perturbation parameter $\varepsilon = C\pi^2/(2\Delta_a^2 \cdot \min_i w_i)$. By Rouché’s theorem [32, 8], if $\varepsilon < 1$ then F_{true} and F_{lin} have the same number of zeros inside the strip $|\text{Im}(\tau)| < \pi/\Delta_a \cdot (1 - \varepsilon)$. This gives:

Proposition Appendix 1.1 (Linearization quality). *Let ν be the unit step direction, $\Delta_a = \max_i a_i - \min_i a_i$ the logit-derivative spread, $\rho_a = \pi/\Delta_a$ the conservative linearized bound, and ρ_{true} the true convergence radius. If the logit curvature $C = \max_i \|d^2 z_i/d\theta^2\|$ along ν satisfies $\varepsilon = C\pi^2/(2\Delta_a^2 \cdot \min_i w_i) \ll 1$, then $\rho_{\text{true}} \geq \rho_a(1 - \varepsilon)$.*

The criterion $\varepsilon \ll 1$ says: the logit Hessian must be small relative to Δ_a^2 , after accounting for the weakest exponential weight in the local partition sum. Residual connections help by keeping C moderate: skip connections keep the logit response approximately linear. Networks without residual connections, such as very deep CNNs, can have large C , degrading the approximation.

Why moderate error suffices. The instability condition $r = \tau/\rho_a \gg 1$ is robust to constant factors in ρ_a . If the linearized radius is off by a factor of 2, the qualitative prediction (safe vs. dangerous) is unchanged whenever $r > 2$ or $r < 0.5$. The theory does not need ρ_a to be exact; it needs the right order of magnitude.

Appendix 1.2 Multi-Step and Stochastic Extensions

Appendix 1.2.1 Single-step suffices for detection

The theory provides a conservative *sufficient* condition for one-step reliability: $\tau < \rho_a$ keeps the step inside the guaranteed local convergence region of the linearized softmax model. Crossing this bound places the update in a hazard regime where the local Taylor approximation need not converge, but it is not by itself a theorem of full-training divergence. Capping $\tau \leq \rho_a$ at every step therefore enforces a local one-step safety condition, not a proof of global convergence.

The theory does not guarantee multi-step convergence. After a safe step, ρ_a may decrease (as confidence grows). The controller handles this by recomputing ρ_a at each step.

Appendix 1.2.2 Stochastic gradients

Mini-batch noise changes ν , hence Δ_a . Empirically, Δ_a varies little across batches (coefficient of variation $\sim 1\%$), so stochastic fluctuation is negligible.

Appendix 1.3 Failure Modes

Appendix 1.3.1 Non-analytic activations

ReLU networks are piecewise linear, not analytic. In the ReLU models tested in this paper, the output-side softmax bound ρ_a still tracked instability usefully, suggesting that softmax ghosts can remain an informative hazard scale even when activation kinks are present. That is an empirical observation about the tested architectures, not a general theorem that softmax singularities always dominate piecewise linear obstructions. A rigorous extension to piecewise analytic or kinked networks remains open.

Appendix 1.3.2 Scale

All experiments use small models (up to 128 dimensions, 10 classes). For large-vocabulary models (50,000+ classes), Δ_a will be larger, making ρ_a smaller. Whether large language models (LLMs) operate perpetually at $r \gg 1$ through favorable cancellation, or whether the linearization slack scales favorably with vocabulary size, is unknown.

Appendix 1.3.3 Comparison to simpler heuristics

The framework improves on a generic “reduce LR when logits are large” heuristic in two ways: (i) it provides the specific formula $\rho_a = \pi/\Delta_a$ with the principled threshold $r = 1$, and (ii) it connects this threshold to Taylor convergence, explaining *why* large derivative spreads cause instability. Whether this quantitative threshold provides practical advantages over simpler rules at production scale remains to be tested.

Appendix 2. Activation Singularities

Section 4 derived the loss radius by linearizing the logits $z_k(\tau) \approx z_k(0) + a_k\tau$ and locating zeros of the partition function. That linearization assumes every component between parameters and logits—including activations—is analytic. Activation functions can have complex singularities of their own, and these can cap the loss radius before the softmax ghosts do. We apply the same lens to feed-forward network (FFN) activations, which can introduce softmax-like ghosts into the network.

Appendix 2.1 Per-neuron radius

For a scalar activation ϕ , let $\Sigma_\phi \subset \mathbb{C}$ denote the singular or nonanalytic set of its complex continuation. Consider neuron j with preactivation $h_j \in \mathbb{R}$. Along the update direction, it evolves as $h_j(t) = h_j + t\dot{h}_j$, and $\phi(h_j(t))$ first becomes singular when $h_j + t\dot{h}_j \in \Sigma_\phi$. Here $\dot{h}_j = \frac{d}{dt}h_j(\theta + t\nu)|_{t=0} = \nabla_\theta h_j \cdot \nu$ is the directional derivative of the preactivation. We compute all \dot{h}_j values simultaneously using one forward-mode

AD Jacobian–vector product along ν . The activation-limited directional radius for that neuron is

$$\rho_j = \min_{s \in \Sigma_\phi} \frac{|s - h_j|}{|\dot{h}_j|}, \quad (21)$$

and the FFN radius is $\min_j \rho_j$. Since the loss depends on the activations through composition, a singularity in any neuron propagates to the loss. Thus the overall convergence radius cannot exceed $\min_j \rho_j$.

Under the same logit linearization used throughout this paper, the activation radius and the softmax radius $\rho_a = \pi/\Delta_a$ give two separate upper bounds. A conservative combined bound is $\min(\min_j \rho_j, \rho_a)$.

Note the asymmetry: $\rho_a = \pi/\Delta_a$ carries a factor of π because partition-function zeros lie at imaginary distance exactly π (the condition $e^{i\pi} = -1$). The per-neuron radius ρ_j has no universal π ; its scale is set by whichever singularity in Σ_ϕ lies nearest to the current preactivation. For sigmoid that distance happens to be π , for tanh it is $\pi/2$, and for ReLU it can be arbitrarily small. The two radii therefore measure different geometric constraints: ρ_a bounds how far one can step before exponential sums in the partition function cancel, while ρ_j bounds how far before a hidden-layer nonlinearity encounters its own complex singularity.

Comparing activation families therefore reduces to one question: where is Σ_ϕ ?

Appendix 2.2 Activation families

Piecewise activations (ReLU, Leaky ReLU, parametric ReLU (PReLU), Hard-Swish, Hard-Sigmoid, ReGLU—a gated linear unit (GLU) variant with ReLU gate). Σ_ϕ lies on the real axis at the breakpoints. The local radius is the distance to the nearest breakpoint:

$$\rho_j = \min_{b \in \mathcal{B}_\phi} \frac{|h_j - b|}{|\dot{h}_j|},$$

For ReLU the main breakpoint is 0, giving $\rho_j = |h_j|/|\dot{h}_j|$. In normalized networks many preactivations lie near break surfaces, so $\min_j \rho_j$ is often small. Piecewise-linear functions are not analytic at their kinks: they lack a Taylor series there entirely. This is a stricter failure than complex singularities off the real axis. This class is cheap and works well in practice, but from the convergence radius lens it is structurally the worst.

Sigmoid family This includes sigmoid, softplus, sigmoid linear unit (SiLU/Swish) [33], and SwiGLU (Swish-gated linear unit) [34]. The logistic function $\sigma(z) = 1/(1 + e^{-z})$ has poles where $1 + e^{-z} = 0$, i.e. $z = i\pi(2k + 1)$ for integer k ; SiLU gates built from it share these poles. Softplus $\text{softplus}(z) = \log(1 + e^z)$ has branch points where $1 + e^z = 0$,

i.e. at the same locations. The nearest singularity lies at imaginary distance π —the same ghost lattice as the softmax partition zeros. This family is much better than ReLU, but it still imposes a hard finite cap from the $i\pi(2k+1)$ lattice. In the language of this paper, these activations bring softmax-like ghosts into the FFN.

Tanh family (tanh, anything built from tanh, including tanh-approximate Gaussian error linear unit (GELU)). $\tanh(z) = \sinh z / \cosh z$ has poles where $\cosh z = 0$, i.e. $z = i(\pi/2 + \pi k)$. The nearest pole is at imaginary distance $\pi/2$, strictly closer than the sigmoid family. This matters because many “smooth ReLU” implementations use tanh-based approximations. In particular, exact GELU and tanh-approximate GELU are analytically different objects: the approximation loses the main structural advantage of exact GELU.

Entire activations (exact GELU [35], exact GeGLU (GELU-gated linear unit), erf-based gates). Exact GELU is $x\Phi(x)$, where Φ is the Gaussian cumulative distribution function (CDF) built from the entire function erf. Thus $\Sigma_\phi = \emptyset$: there is no finite activation singularity. From the convergence-radius viewpoint, this class is structurally strongest because the activation contributes no finite ghost barrier.

Appendix 2.3 Ranking

Based on singularity distance alone, for vanilla FFNs:

$$\underbrace{\text{exact GELU / erf-based}}_{\Sigma=\emptyset} > \underbrace{\text{SiLU, softplus}}_{\pi} > \underbrace{\text{tanh}}_{\pi/2} > \underbrace{\text{ReLU}}_{\text{real axis}}$$

For gated FFNs, the same ordering applies to the gate: exact GeGLU or entire erf-gated GLU > SwiGLU > ReGLU. The main caveat is that exact versus approximate GELU matters.

Caveat: entire \neq unbounded step. A nonconstant entire function cannot be bounded on all of \mathbb{C} . For example, $\text{erf}(z)$ grows as $\exp(z^2)$ off the real axis. So “infinite activation radius” does not mean arbitrarily large steps are safe. It only means the activation itself contributes no finite singularity barrier. The softmax radius ρ_a and the growth rate in the relevant complex strip remain as separate constraints.

Appendix 2.4 Exact vs. approximate GELU

The common tanh approximation

$$\text{GELU}(x) \approx \frac{1}{2}x(1 + \tanh(\sqrt{2/\pi}(x + 0.044715x^3)))$$

reintroduces tanh poles. This seemingly harmless shortcut introduces artificial complex singularities that the exact implementation avoids. Many modern frameworks provide exact erf-based GELU, but legacy codebases and some hardware paths still use the tanh approximation.

Appendix 2.5 Designing radius-friendly components

The ranking above suggests a design principle: prefer entire activations (no finite singularities) over sigmoid-family or piecewise ones. Section Appendix 3 develops this idea, proposing RIA (Rectified Integral Activation, ReLU convolved with a Gaussian) for vanilla FFNs, GaussGLU (Gaussian cumulative distribution function (CDF) gate) for gated FFNs, and an analytic normalization layer via the Weierstrass transform. These are suggestions from the theory, not claims of optimality.

Appendix 2.6 Limitations of this extension

The per-neuron radius (21) is a necessary condition, not a sufficient one. Cancellations across neurons could make the actual loss radius larger. For ReLU, the framework requires reinterpretation since piecewise-linear functions are not analytic. A full treatment, including composition theorems for how activation and softmax radii interact beyond linearization, is left to future work.

Appendix 3. Activation Design from the Radius Lens

Under the convergence-radius lens, an ideal activation would:

1. **Entire.** Have no finite complex singularities, or at least singularities far from the real axis.
2. **ReLU-like on \mathbb{R} .** Suppress the negative side while remaining approximately linear on the positive side.
3. **Monotone derivative.** Avoid dead regions and the mild nonmonotonicity of exact Gaussian error linear unit (GELU).
4. **Controlled strip growth.** Grow moderately for $z = x + iy$ when $|y|$ is in the range relevant to update steps.
5. **Cheap and stable to implement.** Avoid tanh approximations that reintroduce poles.

A nonconstant entire function cannot be bounded on all of \mathbb{C} . So the target is not a globally bounded activation, but one that is entire, ReLU-like on \mathbb{R} , and has mild growth in the relevant complex strip.

Vanilla feed-forward network (FFN): RIA (Rectified Integral Activation). A first-principles design that satisfies these criteria is RIA, the integral of the Gaussian cumulative distribution function (CDF)—equivalently, ReLU convolved with a Gaussian:

$$\phi_\beta(x) = \int_{-\infty}^x \Phi(\beta t) dt = x \Phi(\beta x) + \frac{1}{\beta} \varphi(\beta x), \quad (22)$$

where φ is the Gaussian probability density function (pdf) and Φ is its cumulative distribution function (CDF). This is exactly ReLU convolved with a Gaussian—the cleanest way to remove the kink while pushing singularities to infinity. Its properties: $\phi'_\beta(x) = \Phi(\beta x) \in (0, 1)$, so it is monotone increasing; $\phi''_\beta(x) = \beta \varphi(\beta x) > 0$, so it is strictly convex; $\phi_\beta(x) \rightarrow 0$ as $x \rightarrow -\infty$ and $\phi_\beta(x) \sim x$ as $x \rightarrow +\infty$; and since Φ and φ are entire, ϕ_β is entire. As $\beta \rightarrow \infty$ it recovers ReLU; at finite β it has the qualitative shape of softplus but without the $i\pi(2k+1)$ ghost lattice.

Gated FFN: GaussGLU. For gated FFNs, using $g_\beta(x) = \Phi(\beta x)$ as the gate instead of sigmoid defines GaussGLU:

$$\text{GaussGLU}_\beta(x) = (W_\nu x) \odot \Phi(\beta W_g x). \quad (23)$$

This is the radius-clean analogue of SwiGLU (Swish-gated linear unit): SwiGLU inherits the logistic poles at $i\pi(2k+1)$, while GaussGLU has no finite singularities from its gate.

Appendix 3.1 Analytic normalization

The same principle applies to normalization layers. Layer normalization (LayerNorm) and root mean square normalization (RMSNorm) use the scale factor $f(\nu) = 1/\sqrt{\nu}$, which has a branch-point singularity at $\nu = 0$. Applying the Weierstrass transform (Gaussian convolution) to the thresholded version $f(\nu) = 1/\sqrt{\max(0, \nu)}$ yields

$$\tilde{f}_\sigma(\nu) = \frac{1}{\sigma\sqrt{2\pi}} \int_0^\infty \frac{1}{\sqrt{t}} e^{-(\nu-t)^2/(2\sigma^2)} dt. \quad (24)$$

Because the Gaussian is entire and the integrand is absolutely integrable, this integral defines an *entire function* of ν . Consequently, the singularity at $\nu = 0$ is removed.

Closed form. The integral (24) equals

$$\tilde{f}_\sigma(\nu) = C e^{-\nu^2/(4\sigma^2)} D_{-1/2}(-\nu/\sigma),$$

where C is a constant and $D_{-1/2}$ is a *parabolic cylinder function* (solution of Weber’s equation). Parabolic cylinder functions are entire: no poles, no branch cuts.

Implementation. Deep-learning frameworks lack a native differentiable parabolic cylinder function. Three practical routes exist:

1. **Taylor series.** Since \tilde{f}_σ is entire, its Maclaurin series converges everywhere; precompute coefficients offline and evaluate a truncated polynomial at runtime.
2. **Randomized smoothing.** Use the identity

$$\tilde{f}_\sigma(\nu) = \mathbb{E}_{\xi \sim \mathcal{N}(0, \sigma^2)} [(\max(0, \nu + \xi) + \epsilon)^{-1/2}];$$

sample ξ in the forward pass to recover the analytic function in expectation.

3. **Goldschmidt iterations.** Approximate $1/\sqrt{\nu}$ by a fixed number of polynomial iterations; the N -step sequence is a polynomial and hence entire.

Remark. The convergence radius framework *suggests* the activation, gating, and normalization designs above; it does not prove they are optimal. Practical components depend on many factors beyond analyticity, including gradient flow, trainability, and hardware efficiency. Whether this theoretical advantage yields measurable stability gains must be tested empirically.

Appendix 4. Kullback–Leibler (KL) Divergence and the Convergence Radius

The main text uses complex analysis to derive $\rho_a = \pi/\Delta_a$: the Taylor series of the loss diverges when the step size τ exceeds the distance to the nearest complex singularity.

This appendix derives the same scale from a completely different mechanism: real analysis of the KL divergence. The KL divergence $\text{KL}(P||Q)$ measures the information lost when approximating distribution P by Q . For an optimizer step, it quantifies how much the softmax output distribution shifts, directly measuring prediction change.

We show that the quadratic approximation to KL is accurate when τ is small on the same $O(1/\Delta_a)$ scale highlighted by the ghost bound. The complex-analysis bound gives $\pi/\Delta_a \approx 3.14/\Delta_a$; the KL crossover lies at or below $1/(4\Delta_a) = 0.25/\Delta_a$ —a roughly 12× gap in the constant. Two unrelated derivations, one using complex zeros and the other using real Taylor remainders, point to the same $O(1/\Delta_a)$ controlling scale despite differing constants. This confirms that Δ_a marks a genuine transition variable, not an artifact of a single analysis method.

Appendix 4.1 Setup

An optimizer step perturbs logits from z to $z + \tau a$, where a is the JVP direction and τ the step size. The softmax distribution shifts from $p(0)$ to $p(\tau)$:

$$p_i(\tau) = \frac{e^{z_i + \tau a_i}}{\sum_j e^{z_j + \tau a_j}} \quad (25)$$

We measure the resulting change in prediction with KL divergence. Define the log-partition function $K(\tau) =$

$\log \sum_i e^{z_i + \tau a_i}$ and let $\Delta_a = \max_i a_i - \min_i a_i$ be the logit-derivative spread.

Appendix 4.2 KL as a Bregman Divergence

For exponential families, KL has an elegant form. Along the path $\tau \mapsto p(\tau)$, it equals the Bregman divergence of the log-partition:

$$\text{KL}(p(\tau) \| p(0)) = K(\tau) - K(0) - \tau K'(0) \quad (26)$$

This is the gap between $K(\tau)$ and its linear approximation at $\tau = 0$. The derivatives of K are the cumulants: $K'(\tau) = E_\tau[a]$ (mean), $K''(\tau) = \text{Var}_\tau(a)$ (variance), $K'''(\tau) = E_\tau[(a - \mu_\tau)^3]$ (skewness).

Appendix 4.3 Quadratic Approximation

Taylor-expand $K(\tau)$ to second order with Lagrange remainder:

$$K(\tau) = K(0) + \tau K'(0) + \frac{\tau^2}{2} K''(0) + \frac{\tau^3}{6} K'''(\xi) \quad (27)$$

Substituting into the Bregman formula, the constant and linear terms cancel:

$$\text{KL}(p(\tau) \| p(0)) = \frac{\tau^2}{2} \text{Var}_{p(0)}(a) + \frac{\tau^3}{6} K'''(\xi) \quad (28)$$

The leading term is quadratic—proportional to the variance of the slopes under the base distribution. The cubic remainder determines when this approximation fails.

Appendix 4.4 Sharp Bound on the Remainder

Since a lies in an interval of width Δ_a , we can bound the third cumulant $K'''(\xi) = E_\xi[(a - \mu_\xi)^3]$.

Lemma Appendix 4.1 (Sharp third moment). *For any distribution on an interval of width Δ , $|E[(X - EX)^3]| \leq \Delta^3 / (6\sqrt{3})$.*

Proof. The extremum is a two-point distribution at endpoints. Setting $X \in \{0, \Delta\}$ with $P(X=\Delta) = p$, we get $E[(X - EX)^3] = \Delta^3 p(1-p)(1-2p)$. Maximizing over p gives $p^* = (3 \pm \sqrt{3})/6$, yielding $1/(6\sqrt{3})$. \square

Theorem Appendix 4.2 (Sharp KL remainder). *For softmax distributions $p(\tau)$ with logits $z + \tau a$, step size τ , and logit-derivative spread $\Delta_a = \max_i a_i - \min_i a_i$:*

$$\left| \text{KL}(p(\tau) \| p(0)) - \frac{\tau^2}{2} \text{Var}_{p(0)}(a) \right| \leq \frac{|\tau|^3 \Delta_a^3}{18\sqrt{3}} \quad (29)$$

The constant $1/(18\sqrt{3}) \approx 0.032$ is sharp.

Appendix 4.5 Connection to the Convergence Radius

The quadratic approximation is accurate when the cubic remainder is small compared to the quadratic term: $|\tau|^3 \Delta_a^3 \ll \tau^2 \text{Var}(a)$, i.e. $|\tau| \ll \text{Var}(a) / \Delta_a^3$. Using Popoviciu's inequality [36], $\text{Var}(a) \leq \Delta_a^2 / 4$, so this crossover lies at or below $1/(4\Delta_a)$. The KL analysis therefore points to an $O(1/\Delta_a)$ scale, matching the order of $\rho/\pi = 1/\Delta_a$ but not the exact constant π/Δ_a .

Two derivations, one scale.

- **Complex analysis** (main text): Taylor series of $K(\tau) = \log \sum_i e^{z_i + \tau a_i}$ converges when $|\tau| < \pi/\Delta_a$
- **Real analysis** (this appendix): KL quadratic approximation is accurate when $|\tau| \ll 1/\Delta_a$

Both involve Δ_a and break down at essentially the same scale. The mechanisms are unrelated: one counts complex zeros, the other bounds real Taylor remainders. They support the same order-of-magnitude story, not the same sharp boundary.

Interpretation. Inside the softmax convergence radius, and more conservatively within the KL quadratic regime, the loss and distribution shift admit simple local approximations. The two analyses identify the same controlling spread Δ_a , but with different constants and guarantees. Together they show that softmax departs from locally quadratic behavior on an $O(1/\Delta_a)$ step-size scale.

Appendix 5. Why Hessian Bounds Miss Cross-Entropy

The main text derives $\rho_a = \pi/\Delta_a$ as the stability limit for cross-entropy optimization. A natural question is how this compares to classical Hessian-based bounds. This appendix shows that Hessian bounds can be wrong by orders of magnitude and explains why.

A common stability heuristic models the loss along a direction v as quadratic:

$$L(\theta + \tau v) \approx L(\theta) + \tau g^\top v + \frac{\tau^2}{2} v^\top H v. \quad (30)$$

For a true quadratic, gradient descent becomes unstable when the step exceeds $2/\lambda_{\max}(H)$. This suggests a bound $\tau \lesssim 2/(v^\top H v)$.

Experiments show that this Hessian-based scale can be wrong by orders of magnitude, especially late in training. The issue is not just non-quadraticity. As margins grow, the *analytic structure* of cross-entropy decouples from local Hessian curvature.

Appendix 5.1 Scalar Cross-Entropy Has Nearby Complex Singularities

Consider the scalar logistic loss:

$$f(x) = \log(1 + e^{-x}), \quad (31)$$

where x is a logit margin. On the real line, f is smooth and convex, with

$$f''(x) = \sigma(x)(1 - \sigma(x)) \leq \frac{1}{4}. \quad (32)$$

For a large margin $x = \delta \gg 1$, the Hessian decays exponentially:

$$f''(\delta) \sim e^{-\delta}. \quad (33)$$

A quadratic model would therefore suggest a safe step size scaling as $\sim e^\delta$.

However, f has complex singularities where $1 + e^{-x} = 0$, located at

$$x = (2k + 1)i\pi. \quad (34)$$

These are logarithmic branch points. The Taylor series of f about a real point δ has a finite radius of convergence:

$$R_x(\delta) = \sqrt{\delta^2 + \pi^2}. \quad (35)$$

Although $f''(\delta)$ vanishes exponentially, $R_x(\delta)$ grows only linearly with δ . Consequently,

$$\frac{1/f''(\delta)}{R_x(\delta)} \sim \frac{e^\delta}{\delta} \quad (\delta \rightarrow \infty). \quad (36)$$

Key point. Local curvature governs the quadratic approximation, but convergence of the full Taylor series is limited by the nearest complex singularity. These quantities have fundamentally different asymptotic behavior.

Appendix 5.2 Training Direction Scales with $R_x/|\Delta_{y,c}|$

If the margin evolves as $x(\tau) = \delta + \Delta_{y,c}\tau$, the per-sample loss is $\ell(\tau) = f(\delta + \Delta_{y,c}\tau)$. The directional curvature and Taylor radius are:

$$\ell''(0) = f''(\delta)\Delta_{y,c}^2, \quad \rho(\delta, \Delta_{y,c}) = \frac{\sqrt{\delta^2 + \pi^2}}{|\Delta_{y,c}|}. \quad (37)$$

A Hessian-based step scales as $e^\delta/\Delta_{y,c}^2$, whereas the true radius scales as $\delta/|\Delta_{y,c}|$. This mismatch grows exponentially unless $|\Delta_{y,c}|$ compensates.

Appendix 5.3 Multiclass Case and Logit-JVP Gaps

For multiclass cross-entropy, the same mechanism appears through the top-2 reduction. Let $\delta = z_y - z_c$ be the margin and $\Delta_{y,c} = a_y - a_c$ its directional slope, where $a(x; \nu)$ is the logit Jacobian-vector product. The Taylor radius is:

$$\rho_i = \frac{\sqrt{\delta_i^2 + \pi^2}}{|\Delta_{y,c,i}|}. \quad (38)$$

Confident samples ($\delta \gg 1$) contribute negligible Hessian curvature yet still limit convergence at ρ_i .

Appendix 5.4 Δ_a/ρ_a Predicts Loss Inflation Onset

Define for a sample x :

$$\Delta_a(x; \nu) = \max_k a_k(x; \nu) - \min_k a_k(x; \nu). \quad (39)$$

For a batch \mathcal{B} , the worst-case spread is:

$$\Delta_{a,\max}(\nu) = \max_{x \in \mathcal{B}} \Delta_a(x; \nu), \quad (40)$$

and the corresponding radius:

$$\rho_a(\nu) = \frac{\pi}{\Delta_{a,\max}(\nu)}. \quad (41)$$

The constant π is exact: $1 + e^{\Delta_a \tau}$ has a zero at $\tau = i\pi/\Delta_a$.

Empirically, loss inflation occurs near:

$$r = \frac{\tau}{\rho_a(\nu)} \approx 1, \quad (42)$$

for random directions ν . The Hessian-based scale $2/(v^\top H v)$ is typically 10–100× larger. Across 20 random directions at three training stages (early, middle, and late), we find $\rho_a < 2/\kappa$ in every case. The overestimation grows from $\sim 10\times$ early in training to $\sim 460\times$ late in training, consistent with $\tau_H/\rho_a \propto e^\delta$.

Appendix 5.5 Hessian-to-Ghost Crossover During Training

The empirical findings above show Hessian overestimation growing from $\sim 10\times$ to $\sim 460\times$ during training. We next ask when the Hessian ceases to be binding.

We compare two candidate stability scales at each checkpoint:

Appendix 5.5.1 Quadratic/Hessian scale

For a direction ν , a quadratic model predicts a characteristic step size

$$\tau_H(\nu) = \frac{2}{\kappa(\nu)}, \quad \kappa(\nu) = \nu^\top H \nu. \quad (43)$$

For a worst-case bound, replace $\kappa(\nu)$ by $\lambda_{\max}(H)$.

Appendix 5.5.2 Ghost/ Δ_a scale

Along the same direction ν , define the logit Jacobian-vector product $a(x; \nu) = J_{z(x)}\nu$ and its spread $\Delta_a(x; \nu) = \max_k a_k - \min_k a_k$. The ghost scale is

$$\rho_a(\nu) = \frac{\pi}{\max_{x \in \mathcal{B}} \Delta_a(x; \nu)}. \quad (44)$$

Empirically, one-step loss inflation begins when τ crosses $\rho_a(\nu)$, i.e. when $r = \tau/\rho_a(\nu) \approx 1$, while $\tau_H(\nu)$ often remains much larger late in training. To see when

the Hessian stops binding, consider the top-2 (binary) reduction for one sample:

$$\delta(\tau) = \delta + \Delta_{y,c}\tau, \quad \ell(\tau) = \log(1 + e^{-\delta(\tau)}), \quad (45)$$

where $\delta = z_y - z_c$ and $\Delta_{y,c} = a_y - a_c$. The directional curvature is

$$\ell''(0) = \sigma(\delta)(1 - \sigma(\delta))\Delta_{y,c}^2, \quad (46)$$

which decays as $e^{-\delta}$ for confident samples ($\delta \gg 1$). Thus the quadratic scale $\tau_H \propto 1/\ell''(0)$ grows exponentially with margin, while the ghost/ Δ_a scale $\rho_a \propto 1/|\Delta_{y,c}|$ lacks the saturating factor $\sigma(1 - \sigma)$. Their ratio therefore grows rapidly with confidence:

$$\frac{\tau_H}{\rho_a} \approx \frac{2e^\delta}{\pi|\Delta_{y,c}|}. \quad (47)$$

This predicts a crossover to ghost-dominated one-step reliability once margins exceed

$$\delta^* \approx \ln\left(\frac{\pi|\Delta_{y,c}|}{2}\right), \quad (48)$$

matching the transition point observed in our training-time tracking (Figure 13).

Appendix 5.5.3 Edge-of-stability connection

Across learning rates η , the crossover margin δ^* at convergence follows $\delta^* \approx A + B \ln \eta$ with $R^2 \approx 1$. This is consistent with an edge-of-stability-style mechanism: increasing η requires reducing an effective curvature scale, which cross-entropy can achieve by inflating margins until $\sigma(1 - \sigma)$ becomes sufficiently small. Since $\sigma(1 - \sigma) \sim e^{-\delta^*}$, this yields $\delta^* \propto \ln \eta$.

In this regime, Hessian-based quadratic scales matter less for one-step reliability, while ρ_a continues to predict the observed onset at $r \approx 1$.

Appendix 5.6 Interpretation

The Hessian measures curvature along the real line, which vanishes exponentially for confident predictions. However, the true one-step stability limit is set by complex singularities, captured by $\rho_a(\nu)$.

This explains why adaptive methods that scale by inverse curvature, such as Adam, can become overly aggressive late in training: the Hessian suggests large safe steps, while the convergence-radius bound indicates a nearby singularity.

Connection to main results. This analysis complements the main text. Section 4 derives ρ_a from complex singularities, while this appendix explains why Hessian-based alternatives fail. Section Appendix 4 provides a third derivation using KL divergence bounds. All three approaches converge on the same scale: $1/\Delta_a$.